ITER Fast Ion Collective Thomson Scattering

Detailed integrated design of the collective Thomson scattering (CTS) system for ITER

Bindslev, Henrik; Larsen, Axel Wright; Meo, Fernando; Michelsen, Poul; Michelsen, Susanne; Nielsen, Anders Henry; Nimb, Søren Robert; Tsakadze, Erekle

Publication date:
2005

Document Version
Publisher's PDF, also known as Version of record

EFDA Contract 04-1213 - deliverable 4.1- D3, Final Report

ITER Fast Ion Collective Thomson Scattering

Detailed integrated design of the collective Thomson scattering (CTS) system for ITER

Henrik Bindslev, Axel W. Larsen, Fernando Meo, Poul K. Michelsen, Susanne Michelsen, Anders H. Nielsen, Søren Nimb, Erekle Tsakadze
Association EURATOM - Risø National Laboratory
30 November 2005

1 Introduction

Specifications: *The EU has a strong interest in supplying the collective Thomson scattering diagnostic for ITER. An initial assessment of the optimum frequency range for a collective Thomson scattering system and its integration in ITER has been performed, which shows that collective Thomson scattering is a feasible method to diagnose fast ions including alpha particles in ITER, both in terms of physics and technology. Based on this existing conceptual design, a detailed integrated design needs to be developed.*

The EFDA Contract 04-1213 with Risø National Laboratory concerning a detailed integrated design of a Fast Ion Collective Thomson Scattering (CTS) diagnostic for ITER was signed on 31 December 2004.

In 2003 the Risø CTS group finished a feasibility study and a conceptual design of an ITER Fast Ion Collective Thomson Scattering System (Contract 01.654) [1, 2]. The purpose of the CTS diagnostic is to measure the distribution function of fast ions in the plasma. The feasibility study demonstrated that the only system that can fully meet the ITER measurement requirements for confined fusion alphas is a 60 GHz system. The study showed that with two powerful microwave sources of this frequency (gyrotron) and two antenna systems, one on the low field side (LFS) and one on the high field side (HFS), it should be possible to resolve the distribution function of fast ions both for perpendicular and parallel velocities with good spatial and temporal resolution.

The present report, which is a continuation of this work, presents a detailed CATIA design of the two antennae systems, modified and extended calculations on beam overlap and scattering, measurements and calculations of the beam transmission through the blanket gap, and calculations of diagnosing fuel ion ratio and rotation velocity by CTS.

The fast ion CTS diagnostic on ITER consists of two separate systems. Each system has its own RF launcher and separate set of detectors. The first system shown in Figure 1 measures the perpendicular component of the fast ion velocity distribution. It consists of radially directed RF launcher and receiver, both located in the equatorial port on the low field side (LFS). This system will be referred to by the acronym LFS-BS system referring to the location of the receiver and the fact that it measures backscattered radiation.

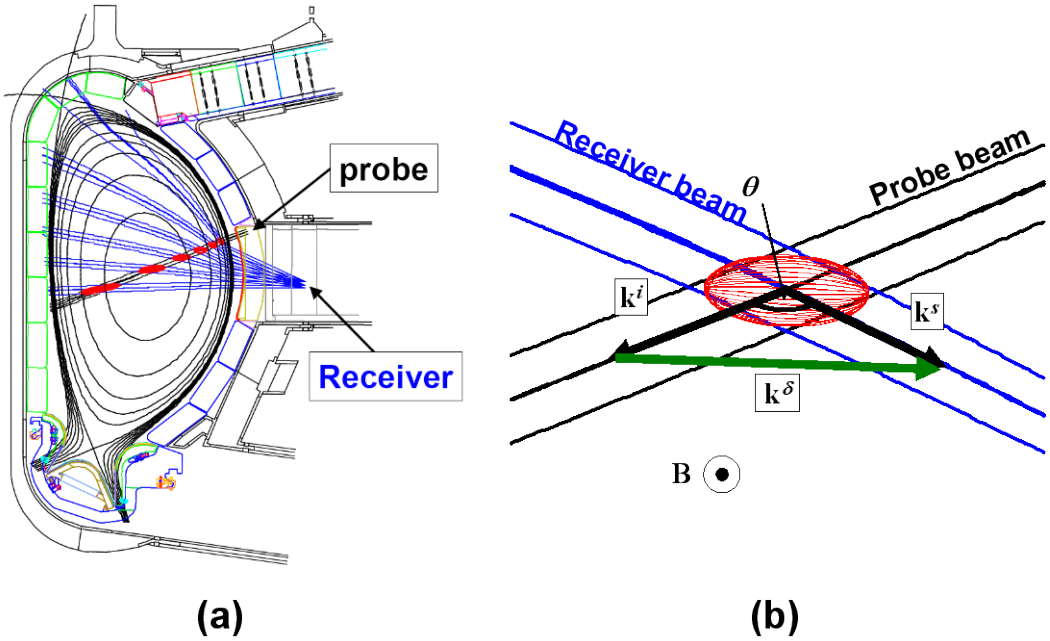

Figure 1. Poloidal view of the Low Field Side – Backcattering (LFS-BS) set-up: (a) Beam traces of the LFS-BS system w.r.t the ITER vessel components. (b): A close up view of the probe beam and one of the receiver beams, the scattering volume (in red). The drawing shows the wave vectors of the received scattered radiation k^s, probe radiation k^i, and the fluctuation wave vector $\boldsymbol{k}^\delta$. ($\boldsymbol{k}^\delta = \boldsymbol{k}^s - \boldsymbol{k}^i$).

The second part of the CTS diagnostic on ITER shown in Figure 2 measures the parallel component of the fast ion distribution. It consists of an RF launcher located in the mid-plane port on the LFS and a receiver mounted on the inner vacuum vessel wall that views the plasma from between two blanket modules. This system will be referred to as HFS-FS referring to the location of the receivers and that they measure forward scattered radiation. The design of both LFS-BS and HFS-FS receivers is aimed at measuring at different spatial locations simultaneously with no moveable components near the plasma.

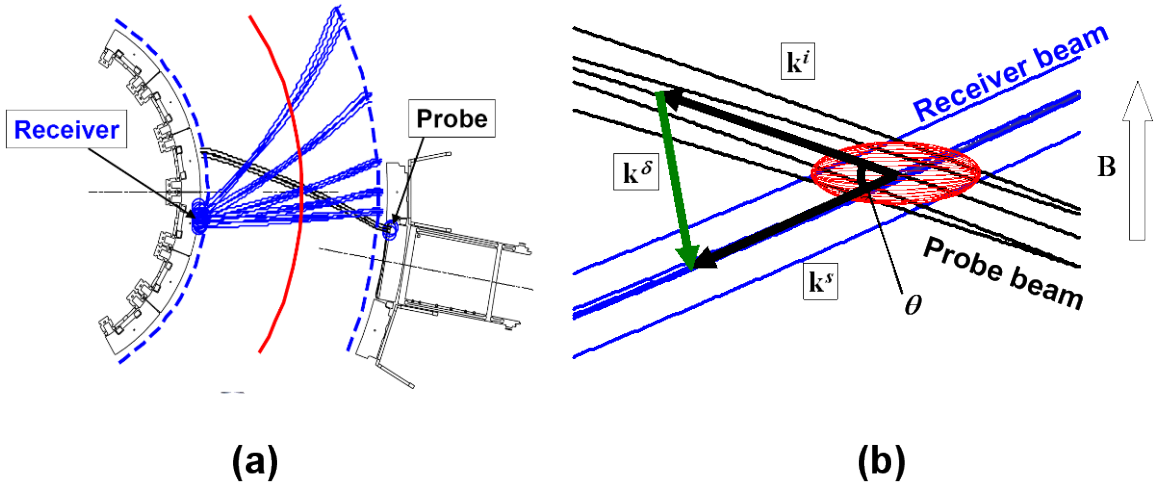

Figure 2. (a) Top view of beam traces for the High Field Side – Forwardscattering (HFS-FS) with a probe launcher on the low field side with detectors located on the HFS. (b) Close up view of the probe beam and one of the receiver beams with the scattering volume (in red). Shown are the wave vectors of the received scattered radiation k^s, the incident probe radiation k^i, and the fluctuation vector $\boldsymbol{k}^\delta = \boldsymbol{k}^s - \boldsymbol{k}^i$ which is near parallel to $\boldsymbol{B}$.

After the introduction, the optimization of design of the HFS receiver system is described in Sec. 2. Overlap and scattering simulations have been performed for the updated HFS-antenna system taking into account the different beam diameters calculated by Gaussian optics for a variety of ITER plasma profile. The results show that the measurement requirements are satisfied with the new mirror position imposed by the various engineering constraints.
In Sec. 3 the detailed design of front-end components carried out in close collaboration with the ITER IT in Garching is first described. Secondly, measurements with a mock-up model designed and constructed at Risø are presented. This mock-up model was built in order to estimate the beam transmission through the slit between the blanket modules on the HFS. The results show that beam transmission through a slit with a width of 300 mm and a vertical opening of 30 mm is possible. A numerical calculation of this problem has until now not been successful. Sec. 4 presents calculations of diagnosing fuel ion ratio and rotation velocity by CTS. The results show that a 60 GHz CTS system can measure the fuel ion ratio and poloidal and toroidal drift velocities with the required accuracy, while it is not obvious that the fuel ion ratio can be estimated with the required accuracy using a probe at 28 THz. Finally in Sec. 5 a list of future task necessary to develop this diagnostic is given.

2 Optimization of present design of the HFS receiver system

2.1 Updated overlap and scattering simulations

Due to the geometrical constraints that will be mentioned in 3.1, the mirror positions for the HFS-FS probe have been modified with respect to those assumed in Ref. 2. As a result, the beam overlap/scattering simulations have been updated to include these changes. In addition, the new simulation studies include beam diameters selected to account for the actual Gaussian beam of each receiver beam that have their beam waist positions at different distances from the receiver mirror. In other words, the overlap/scattering simulation results in the feasibility report [1], assumed all beams have the same beam diameter (Gaussian radius * 3.2) of 20 cm. In the asymptotic limit a Gaussian beam width grows linearly, so it can be represented by a bundel of rays, coming from the beam waist. The Gaussian beams in the beam overlap calculations are represented by a bundle of rays consisting of 5 independent rays; the beam centre and 4 rays, each at one Gaussian half width from the centre. With these 5 rays the refraction of a Gaussian beam is modelled, but not the diffraction. To account to some extent for the diffraction, we choose a bundle of rays that is tangent to the real Gaussian beam in vacuum at the distance from the aperture that is of interest. We use this ray bundle as an approximation to the Gaussian beam locally in the plasma. It, of course, does not account for the plasma modification of the diffraction, which we assume is of modest importance in our studies. For the HFS-FS system, the beam plane is horizontal (see section 3 of reference 2). Hence the vertical dimension of the beams will mainly influence the beam overlap, thus the CTS signal strength, whereas the horizontal dimension will mainly influence the spatial resolution. Figure 3 and Figure 4 show the beam dimensions of the receiver (horizontal only) and probe, respectively [2].

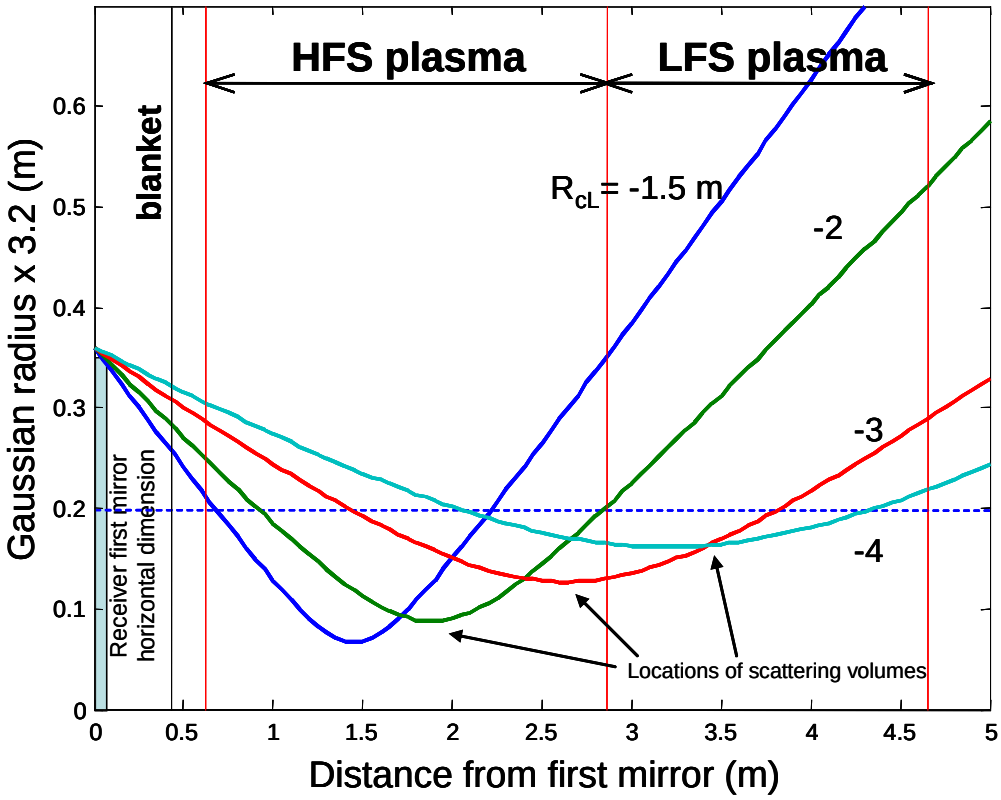

Figure 3. Horizontal properties for the HFS-FS receiver beam (see Figure 2). Beam diameters (Gaussian radius × 3.2) as functions of distance from mirror (located behind the HFS blanket) for different radii of curvature, R_{cl}, (in meters) at the mirror. The vertical red lines represent the position of the boundaries of different plasma regions. The vertical black line represents the position of the blanket. The horizontal dashed line represents the beam diameter upper limit that will still satisfy the measurement requirements for the fast alphas. The mirror size is 360 mm and the frequency of the Gaussian beam is 60 GHz. The negative values of the radii of curvature indicate that the beams are focusing toward the plasma.

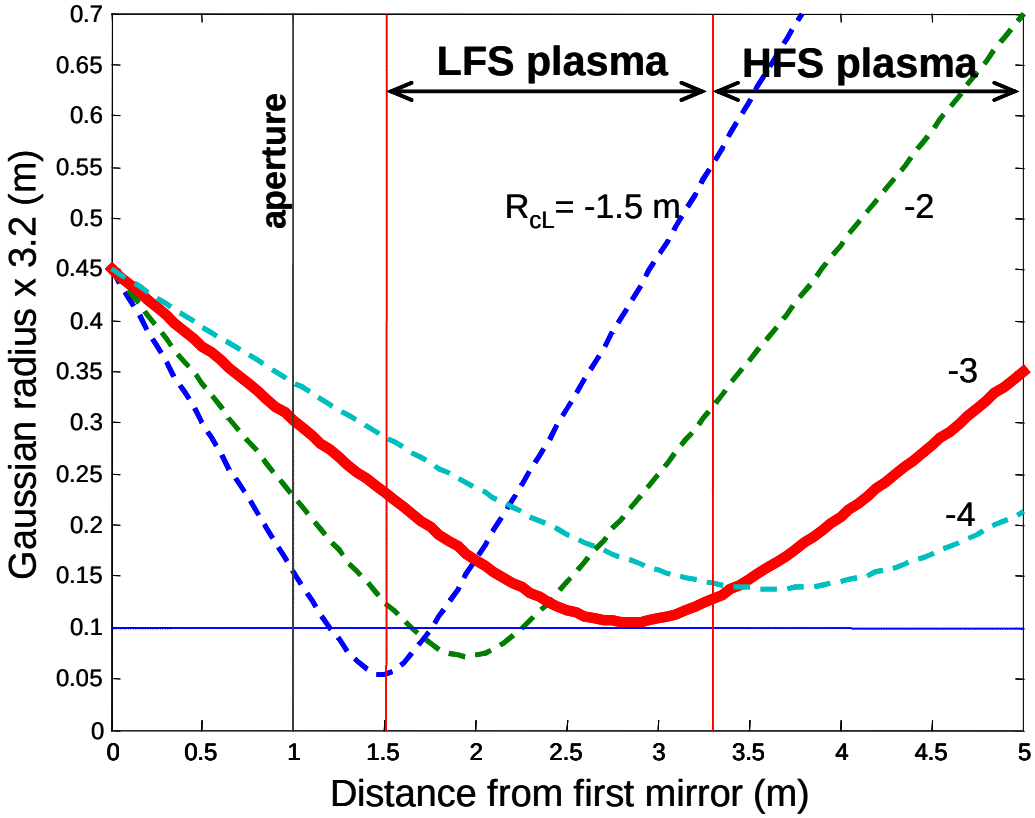

Figure 4. Horizontal and vertical beam properties for the HFS-FS probe (see Figure 2). Beam diameters (Gaussian radius × 3.2) as functions of distance from mirror (located in the port plug) for different radii of curvature, R_{cl}, (in meters) at the mirror. The vertical red lines represent the position of the boundaries of different plasma regions. The vertical black line represents the position of the blanket. The mirror size is 450 mm and the frequency of the Gaussian beam is 60 GHz. The negative values of the radii of curvature indicate that the beams are focusing toward the plasma

In the overlap/scattering simulations, we will refer to the resolving power, L, which was defined and discussed in Ref 1 (section 1.8). It is a measure of the accuracy with which the system can estimate the fast ion velocity distribution for a given velocity space resolution. For all systems discussed in this report, a minimum resolving power of 4 is selected. This corresponds to requiring that the systems resolve at least L2 = 16 orthogonal components of the fast ion velocity distribution, essentially points in the fast ion distribution, with an uncertainty, σ, smaller than the target accuracy, $\Delta = 6\times10^{9}$s/m^{4}. For comparison, we show the resolving power in Figure 5 calculated from the feasibility report [1]. The electron density is scaled from the reference plasma used in the simulation by the factor DS. The updated overlap/scattering simulations, shown in Figure 6, use the horizontal diameter for each receiver beam equal to the waist depicted in Figure 3 and the beam probe diameter at the position where the scattering volume is located (shown in Figure 4). The results clearly show an improvement in the spatial resolution and little influence on the CTS signal as expected.

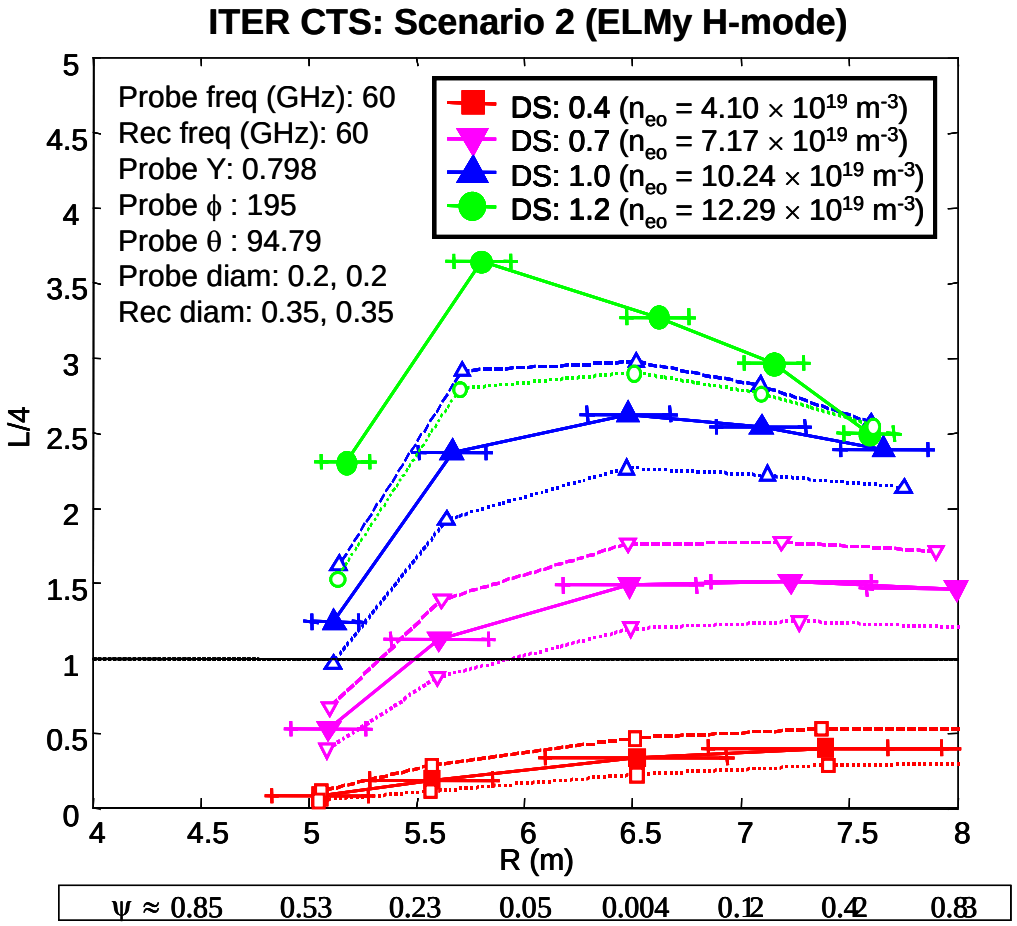

Figure 5. Resolving power, L/4, for the fusion alphas against the radial location of the scattering volume as derived in Ref. 1. Each colour and symbol represents a plasma density by scaling reference plasma density by the factor DS. The dashed and dotted lines are respectively the results of +10% and -10% changes in the density caused by sudden events such as sawteeth.

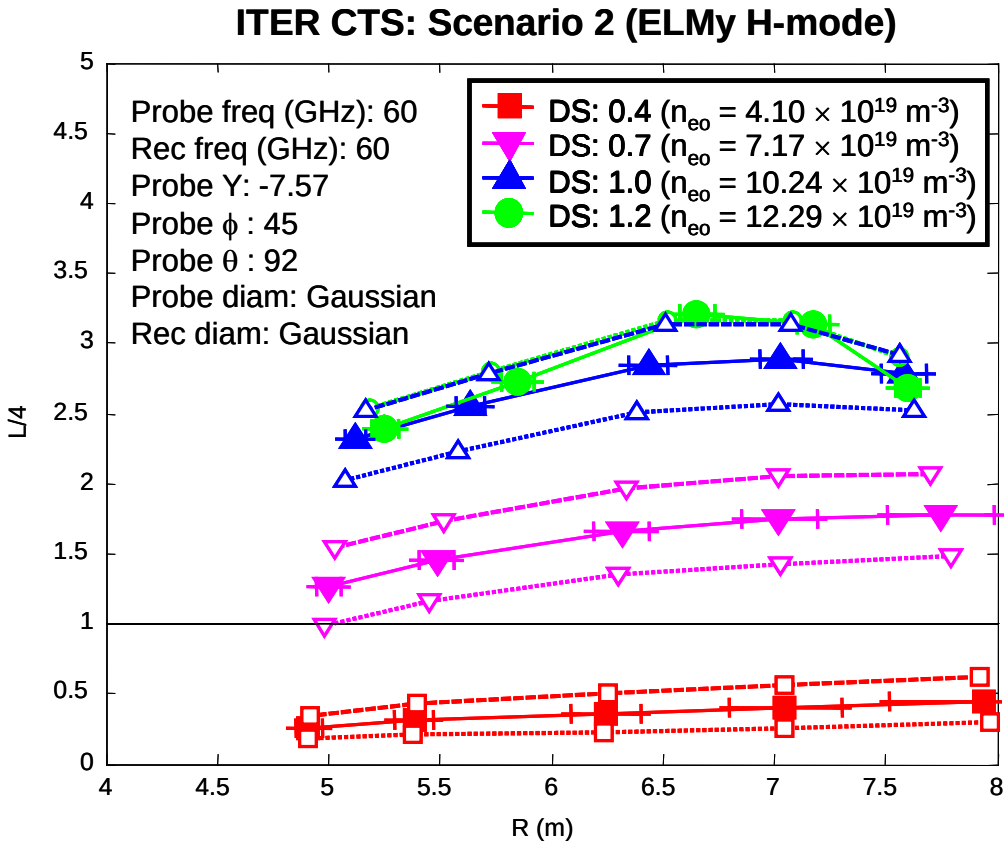

Figure 6. The updated calculations of the resolving power, L/4, for the fast alphas with the new probe location and launch angle. The abscissa is the radial location of the scattering volume. The colour and line type scheme is the same as Figure 5.

The mirror position change has however affected the results for the higher density case (DS=1.2 i.e. 12.3×10^{19} m^{-3}), but is still above the measurement requirements depicted by the horizontal line (L > 4). An additional improvement is the launching angle of the probe. Originally, the probe angle was such that the ECRH power did not directly strike the edge of blankets #3 and 4. This angled launch resulted in the degradation of the signals on the HFS (see Figure 5). However, the diameter of the probe beam expands to about 0.35 m at the blanket thus reducing the power density. To explore this possibility, studies have been done with the beam launch angle around 0-2° from the horizontal. We see from Figure 6 that the resolving power profile is flatter and there is an improvement in the DS = 0.7 (7.17×10^{19} m^{-3}) case. However, due to the poloidal magnetic field causing vertical refraction, the beam probe is about 20 cm below the plasma centre. A remote steering option will add an extra flexibility in the probe launch direction to either optimize the CTS signal profile or to have direct measurements in the plasma centre. Further studies of the effect of direct ECRH power onto the blanket edges need to be made.

2.2 Other ITER scenarios

The overlap/scattering studies in the feasibility studies used the standard Elmy H-mode scenario (appendix A of Ref. 1). The density is scaled by a factor DS to account for variations in operating scenarii. The feasibility report [1] concluded that the 60 GHz based CTS diagnostic can satisfy the measurement requirements for the fast fusion alphas for central density range ≈ 6 - 13.0×10^{19} m^{-3}. In this section, we consider other ITER scenarios with different magnetic configurations and plasma profiles. Before exploring the scenarios, we would like to outline the main factors that influence the CTS signal. The two major factors

influencing the scattered signal are the density and overlap (effectively the scattering geometry). As the reader can already notice from Figure 5 and Figure 6, the density has a major effect on the CTS signal. This is due to the fact that the equation of transfer for a CTS system, describing the spectral power density of the received scattered radiation, in terms of incident probe beam power, is directly proportional to the density [equation 1.1 of Ref 1]. The magnetic topology will influence the beam paths, hence affecting the scattering geometry.

The ITER plasma scenarios [3] considered are listed in Table 1. The weakly reversed shear scenario (Scenario 4) at Ip = 9 MA has been chosen because it has the largest equilibrium difference from the Elmy H-mode standard scenario 2. One can see form Figure 7 that the density profiles are very similar. The resolving power calculations for the reversed shear scenario are shown in Figure 8 at different scaled densities. The results show that even in the reversed shear scenario, the resolving power is above the target value (L/4 > 1) and that are robust against density fluctuations of 10%. Comparing both scenarios (graphs in figures Figure 6 and Figure 8), one can see that the resolving power profiles are flatter in the reverse shear scenario.

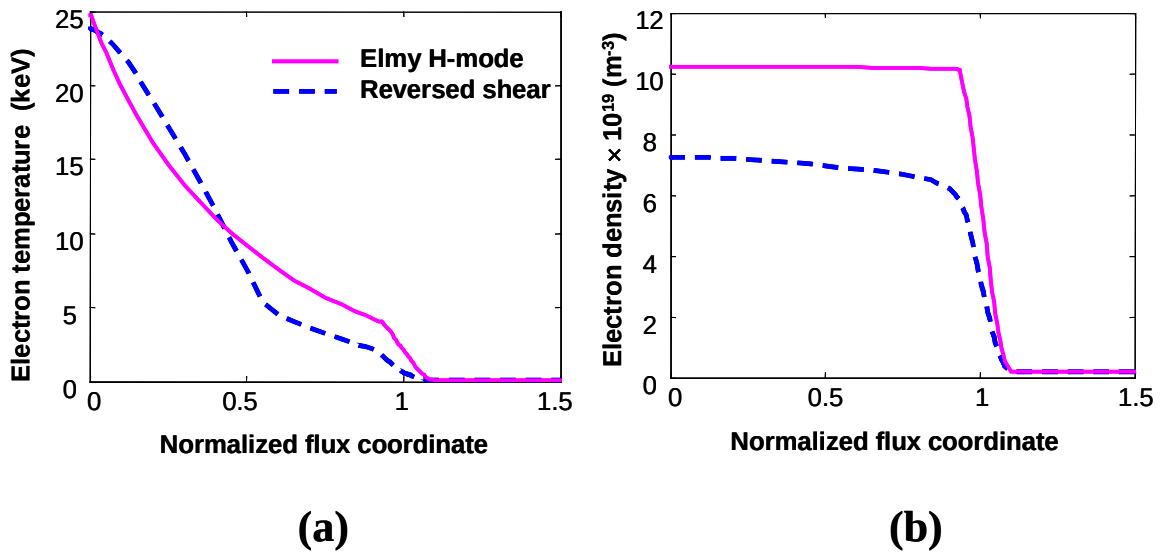

Figure 7. Plasma temperature (a) and density (b) profiles for the standard Elmy H-mode (solid magenta) and reversed shear scenario (dashed blue).

Table 1. Main parameters for ITER scenario taken form the database [3]

Parameter	Standard H-Mode (Scenario 2)	Weakly Reversed shear (Scenario 4)
Bo (T)	-5.3	-5.425
Ne(0) (m^{-3})	10.24×10^{19}	7.27×10^{19}
Te(0) (keV)	24.7	23.9
R_{mag} (m)	6.41	6.66
Z_{mag} (m)	0.68	0.52
Ip (MA)	15	9
β_N	1.842	2.567
βp	0.661	1.529

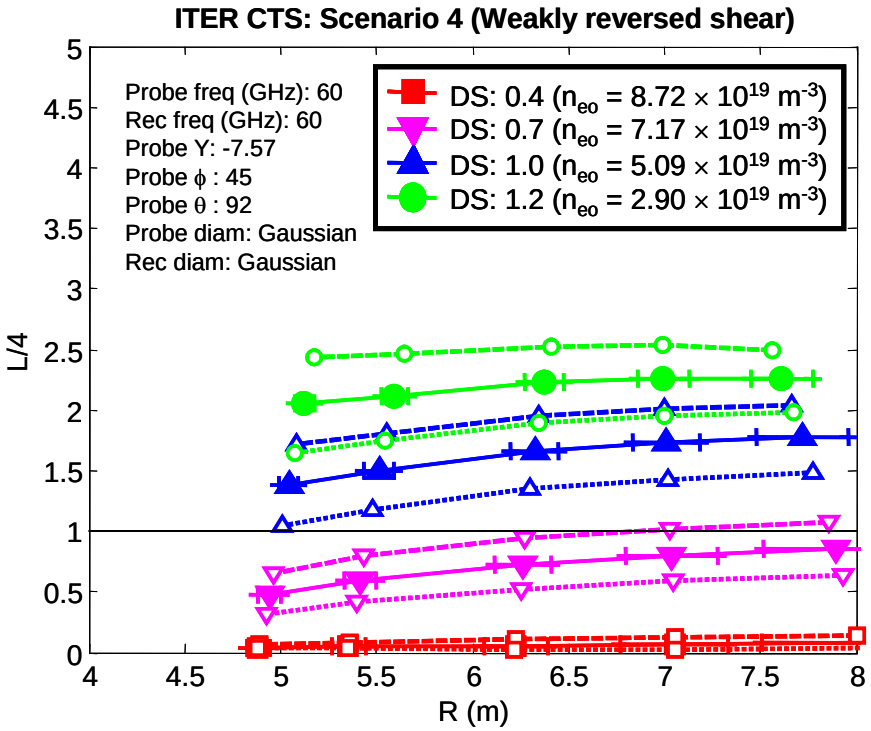

Figure 8. Resolving power, L/4, for the fast alphas for the ITER Scenario 4 (weakly reversed shear) against the radial location of the scattering volume. Each colour and symbol represents a plasma density scaled by the factor DS. The dashed and dotted lines are respectively the results of +10% and -10% changes in the density.

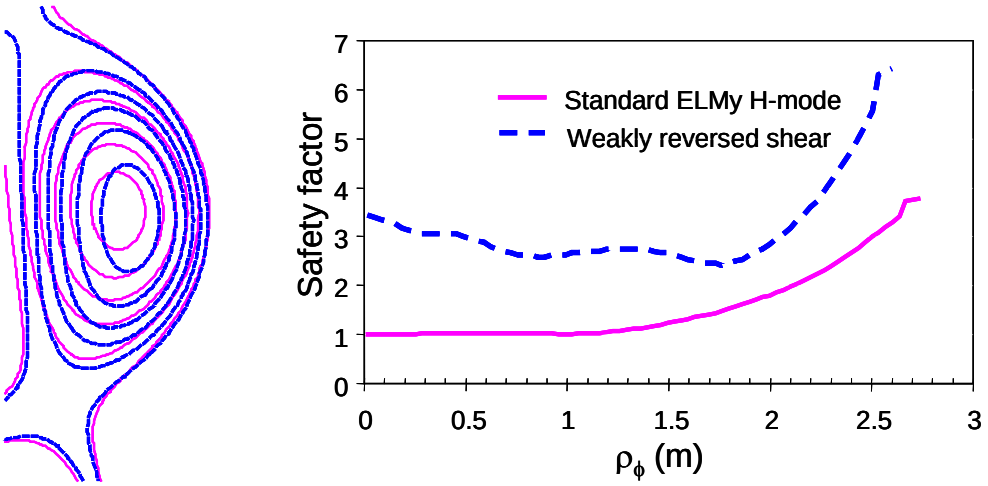

Figure 9. The magnetic surfaces (a) and the safety factor (b) for the standard H-mode scenario (magenta lines) and the weakly reversed shear scenario (blue dashed lines)

The differences in the magnetic equilibriums between the scenarios can be seen in Figure 9. As already mentioned above, the magnetic configuration will influence the beam paths and hence the scattering geometry. To study the effect of the different magnetic configuration on

the resolving power, we scale the density of the reversed shear scenario to equal that of the standard H-mode scenario. The results in Figure 10 demonstrate a marginal effect on the values and the profiles due to magnetic configuration. However, it is important to note that this discrepancy between equilibria becomes larger when the probe launching angle is not optimized.

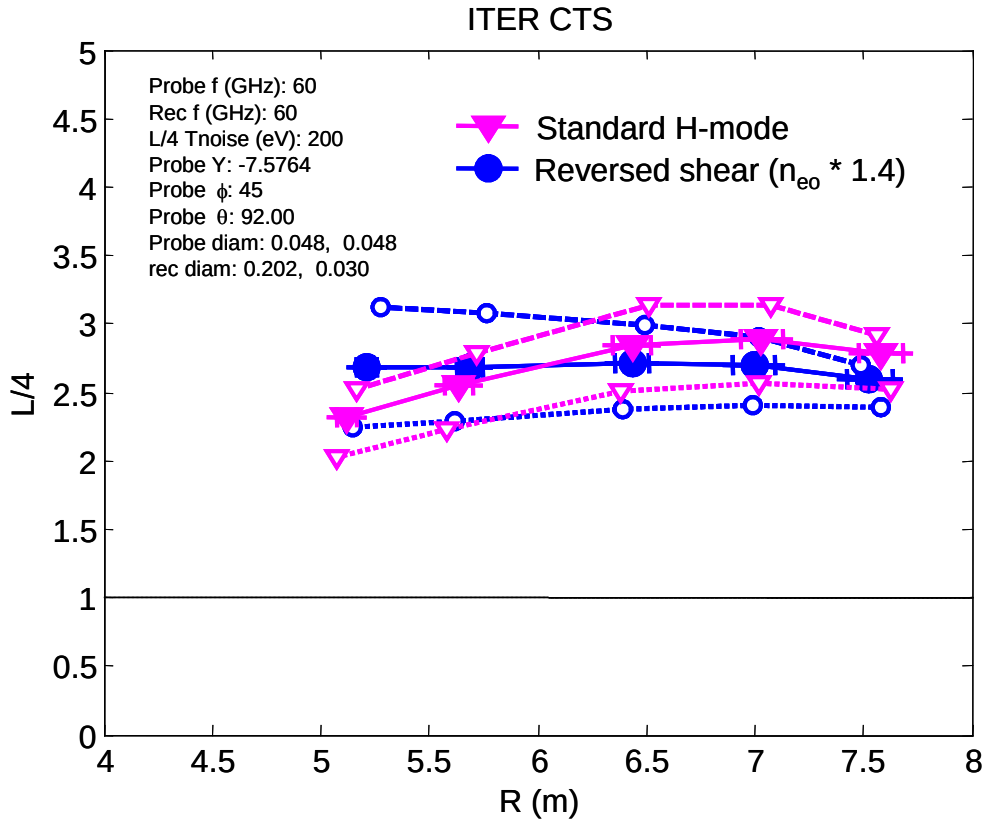

Figure 10. Comparison of the Resolving power, L/4, against the radial location of the scattering volume for two ITER scenarios. The density of the reversed shear scenario has been scaled to equal the density in the standard H-mode. The dashed and dotted lines are respectively the results of +10% and -10% changes in the density.

In summary, we have seen that the measurement requirements are satisfied with the new mirror position imposed by the new engineering constraints. The probe launch angle for the HFS-FS system can be optimized to increase the overlap on the HFS. In fact, studies have shown that this optimized angle makes the CTS less sensitive to changes in scenarios. However the effects of directing ECRH power directly to the blanket edges needs to be further investigated. The overlap/scattering studies have been done for different ITER plasma scenarios, namely the reversed shear at Ip = 9.0 MA. The measurement requirements for the fast fusion alphas are also satisfied in this scenario. We conclude that the different magnetic configuration of scanerio 4 has a marginal effect on the overlap (thus the CTS signal). The parameter that will have the largest effect when choosing an operating scenario is the plasma density.

3 Detailed design of front-end components

This section describes the work with the detailed design of the two antennae systems. First we discuss the constraints for the design. Secondly we describe the detailed design of both the low field side - back scattering (LFS-BS) and the high field side - forward scattering (HFS-FS) antenna systems. In developing the design, three criteria must be satisfied; measurement requirements for the fast ion measurements of the fusion alphas, microwave propagation and hardware, and the engineering constraints imposed by ITER. Before presenting the detailed design, we will outline the three constraints. In order to find suitable solutions for the HFS-FS system, satisfying the severe geometrical constraints, a simple mock-up model was constructed mainly in order to estimate the necessary size of the blanket slot, which the measuring signal has to pass. A numerical model has also been pursued which will be computationally presented in section 3.5. However, due to large dimentions of the system (terms of wavelength), a full wave numerical solution was limited on present-day computers.

3.1 Constraints

The first constraint is the measurement requirements for the fast ion measurements of the fusion alphas as described in Ref.1. The main factors that affect this are the scattering geometry and the beam sizes. The conceptual design report [2] has concluded that the 60 GHz based CTS diagnostic satisfies all measurement requirements under the engineering constraints of ITER.

The second constraint is the microwave propagation and hardware. There is a lower limit to the beam size that can be projected a given distance from a given aperture. The feasibility and conceptual design reports [1,2] concluded that astigmatic beams are needed to satisfy the measurement criteria. The reports only considered the first mirror positions when calculating the beam properties and apertures. This report includes more detailed design (in 3D) of the microwave setup needed to produce the required beams, for example a second mirror, horn dimensions, and distances between them. The quasi-optic design will, of course, be subject to constraints imposed by the limited space and the permissible apertures in the ITER first wall. To study the integration of the astigmatic beams with ITER, 3D astigmatic beams are calculated and imported into the CATIA® [4] models. For the case of the astigmatic Gaussian beams, the symmetry of the beam properties in *xz* and *yz* planes is broken (*z* is the beam propagation axis) and, therefore, the problem of finding the beam parameters can be split in two orthogonal planes, *xz* and *yz*, respectively. The expression for the field distribution in a Gaussian beam is:

$$E(x,y,z)=\left(\frac{2}{\pi w_x w_y}\right)^{0.5}\times exp\left(-\frac{x^2}{w_x^2}-\frac{y^2}{w_y^2}-j\frac{\pi x^2}{\lambda R_x}-j\frac{\pi y^2}{\lambda R_y}+j\frac{\phi_{0x}}{2}+j\frac{\phi_{0y}}{2}-jkz\right),$$

where the beam radii (w_x and w_y), the radius of the curvatures (R_x and R_y) and the Gaussian beam phase shifts (ϕ_x and ϕ_y) are functions of the beam waists (w_{0x} and w_{0y}), wavelength (λ) and the distance on the axis *z* in both *x* and *y* directions, respectively. During the anisotropical Gaussian beam calculations, the values of the w_x and w_y were found in MatLab and the corresponding files were imported into the CTS on ITER CATIA models. An example of a beam calculation is shown in Figure 11. The 3D beam is then incorporated into the design, which will reveal any possible integration issues.

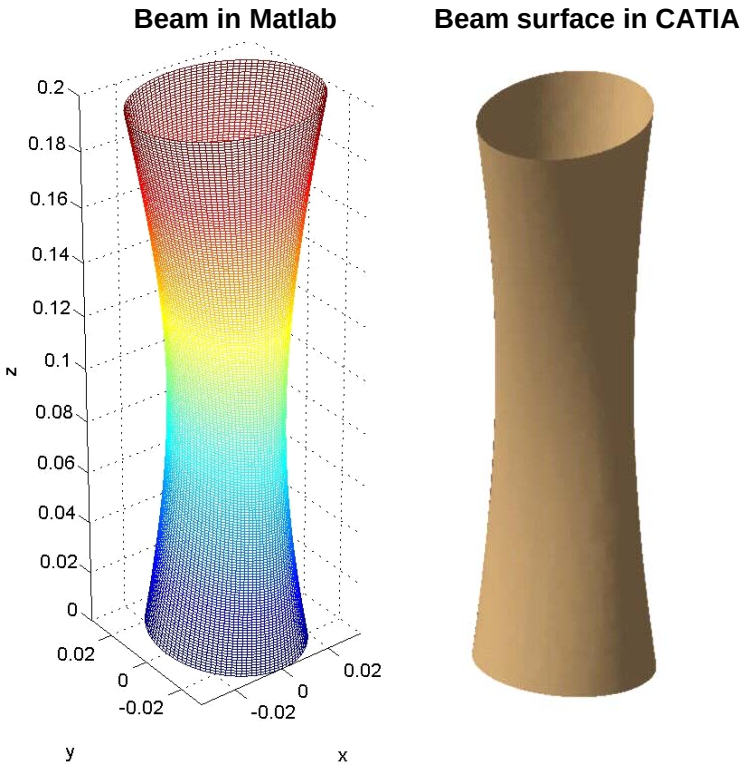

Figure 11. Calculated beams in Matlab (left) and imported into CATIA (right)

The third constraint is the integration into ITER. These constraints do not only involve the hardware and compatibility with other diagnostics, but also the constraints imposed during operation. One example is machine protection from additional neutron flux due to extra blanket apertures, which will be mentioned later in this section.

3.2 LFS-BS system design

Some upgrades to the port plug components have been done during this contract. The updated design is shown in Figure 12. The blanket shield module (BSM) is not shown and the plug front plate outer frame has been made semi-transparent. For structural reasons, apertures in the port plug front plate are limited to the central region and not in the outer portion shown in Figure 12. Due to this extra constraint, the quasi-optical components of the LFS-BS receiver and probe were lowered compared to the previous design in the conceptual report. Due to new constraints from the cooling components of the port plug, the HFS-FS probe first mirror was relocated toroidally. To accommodate the HFS-FS probe Gaussian beam, some portion of the welding edge of the port plug front plate frame has been cut-out. All these modifications of the mirror positions have a direct impact on the scattering geometries, which impact the CTS signal and the radial resolution. However, results from scattering studies with the new mirror locations have concluded that the measurement requirements for the fusion alphas are still satisfied.

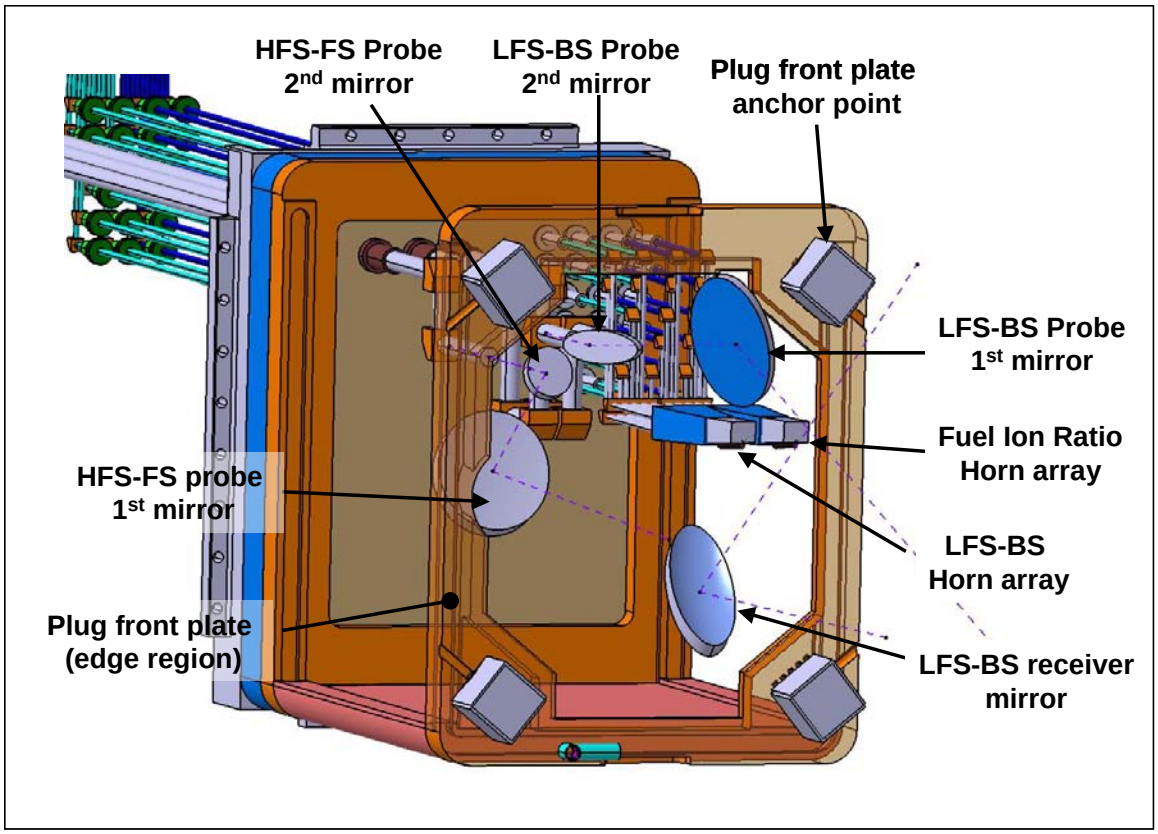

Figure 12. View of the CTS in port plug #12

Figure 13 shows the CTS design in port plug #12 with the 3D Gaussian beams. The two extreme LFS-BS receiver beams are in brown, the LFS-BS probe beam is shown in pink, and the HFS-FS probe beam in light green. The blue ellipses are the scattering volumes at both limits of the measurement.

The apertures in the BSM for the LFS-BS probe and receiver have been combined from the previous design to 273 mm (H) and 1186 mm (V). The updated CTS apertures have also been lowered, thus overlapping the aperture for the visible continuum array diagnostic. However, it is possible for both the CTS and visible continuum to share a common aperture since the visible continuum array diagnostic is located in the centre of the port viewing toroidally. The shape and dimension of this shared aperture is yet to be determined. Finally, the extra horn array and transmission lines for the receiver and probe of the fuel ion ratio diagnostic (see Section 4) have been added to the design as illustrated in Figure 12 and Figure 13.

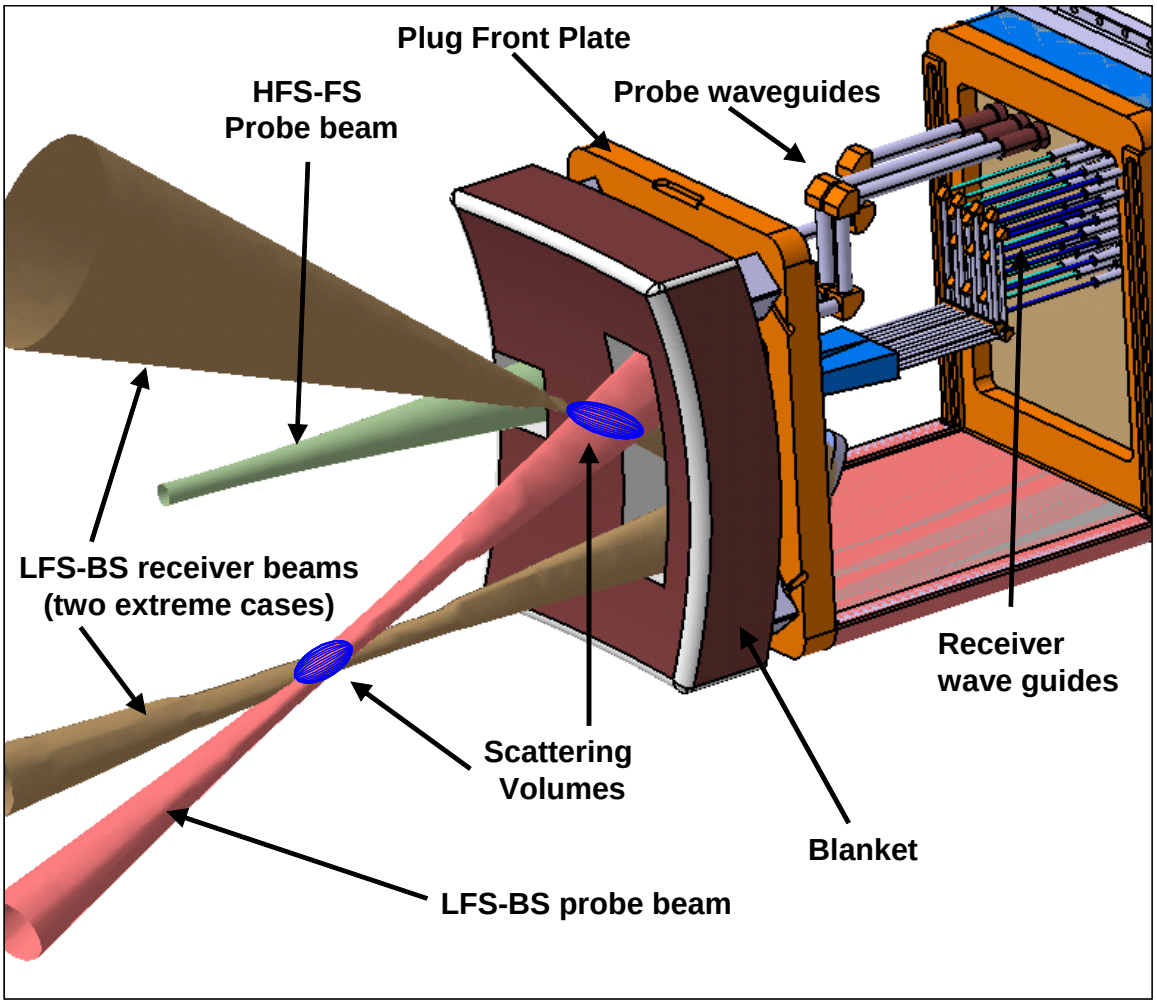

Figure 13. View from the plasma side of the mid-plane port plug #12 with the Gaussian beams. There is inserted doglegs to minimize the neutron streaming. The actual radial locations were not optimized. This will be a part of the coming engineering design task.

3.3 HFS-FS system design

The horizontal and vertical dimensions of the first mirror are limited by the space available between the cooling manifolds and the space between blanket module key and the earth-strap mounting block, respectively. However, the feasibility report has shown that the CTS can satisfy the diagnostic requirements within these constraints. The largest integration issue is the size of the vertical gap between the blankets where the receiver is viewing. Presently the vertical gap in the ITER design is 10 mm. According to the feasibility report [1], the vertical gap should be no less than 30 mm in order to satisfy the measurement requirements taken into account +/- 4 mm the expected tolerances between the blankets. The tolerances and their effect on performance will be studied in the next contract. With the extra spacing, there is the concern of the extra *local* increase of neutron flux on two of the 18 TF coils affected. To reduce this effect, the 30 mm gap has been reduced to produce a “slot” as shown in Figure 14. The horizontal dimension of this slot has been chosen to accommodate the full beam diameter of all beams measuring the different locations in the plasma.

Figure 15 shows the HFS-FS receiver system without the upper blanket #4. The blanket cut-out shown in green, is angled in one direction, where the measurements are taking place. Also shown are the two beams at the limits of the angular coverage needed for the profile (7° and

37° from radial). Due to a blanket module key limiting the vertical position of the first mirror, it was necessary to lower the *effective* slot. Therefore a spacer shown in yellow in Figure 14 has been added to the bottom of blanket #4 and the blanket cut-out is 28 mm which results in an effective slot height of 30 mm +-4mm. .

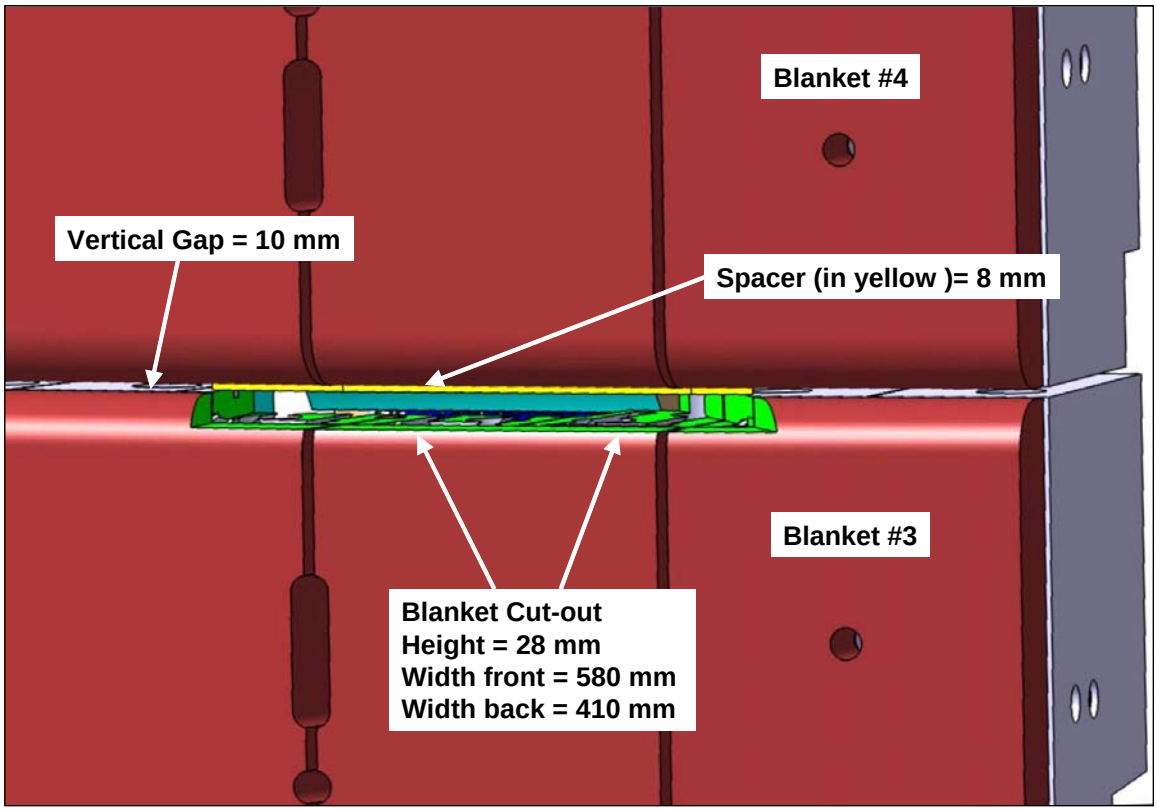

Figure 14. Viewed from the plasma, the inner blanket modules #3 and #4 for the HFS-FS system.

Preliminary simulations have been done [6] to investigate the effect of the slot on the neutron flux. The simulations assumed that the gaps are completely empty and the slot is completely radial. Two scenarios were studied with the vertical gap of 3 cm, and horizontal gaps of 40 and 80 cm. The studies have shown that the total heat increase in both cases is negligible. The mirrors will be mounted on the inner wall, so the heat will be even distributed. This has to studied in detail in the engineering design.

However, the local maximum flux is increased by 50 and 60 % for the horizontal cut of 40 and 80 cm respectively. Further studies need to be done taking into account the extra shielding from the mirror and an angled slot.

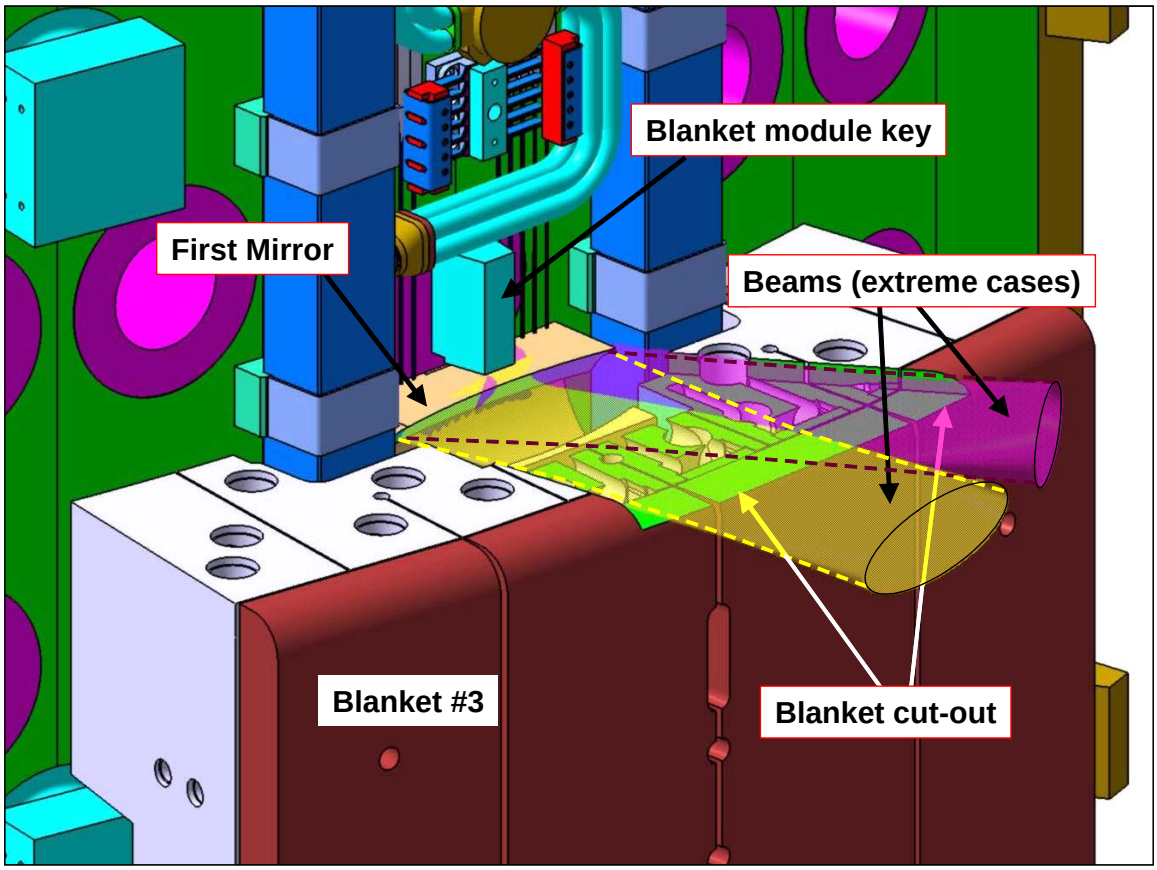

Figure 15. The CTS HFS-FS receiver viewed from the plasma. The blanket #4 is not shown.

The receiver front end is shown in Figure 16. For illustrative purposes, the upper blanket and the cooling manifold are not shown. The front end is a complete unit consisting of two mirrors and a series of horns beneath the second mirror. The unit is mounted on the vacuum vessel and will be independent of the blanket modules. A possible adjustment mechanism to account for installation tolerances of the blankets has to be developed. The unit is cooled by the vacuum vessel wall through conduction. The depth of the unit is about 200 mm. The horns are distributed toroidally, each representing a different toroidal angular view in the plasma. Each horn will be located at the waist of each beam. The distance between the scattered volumes and the first mirror ranges from about 2 to 3 m and the angular range is about 30 degrees. Hence in order to fit 10 horns (the beam waists) a two-mirror approach has been chosen. One scenario is shown in the Gaussian beam calculation plotted in Figure 17. The magenta and blue curves are the horizontal and vertical beam diameters, respectively. The beam waist in the vertical dimension is located at the blanket gap and represents an expanding beam from a vertical gap of 30 mm as calculated by the full wave code [1]. Another advantage of using two mirrors is the added flexibility to shape the beams into a circular horn. The horizontal lines shown are the limits of the mirror sizes imposed by the space available. The horizontal limit imposed by the space between the cooling manifolds is about 350 mm. The vertical limit is imposed by the expanding beam and the space available below the blanket modules key. Further studies of a possible one mirror solution and optimized two mirror solutions need to be done.

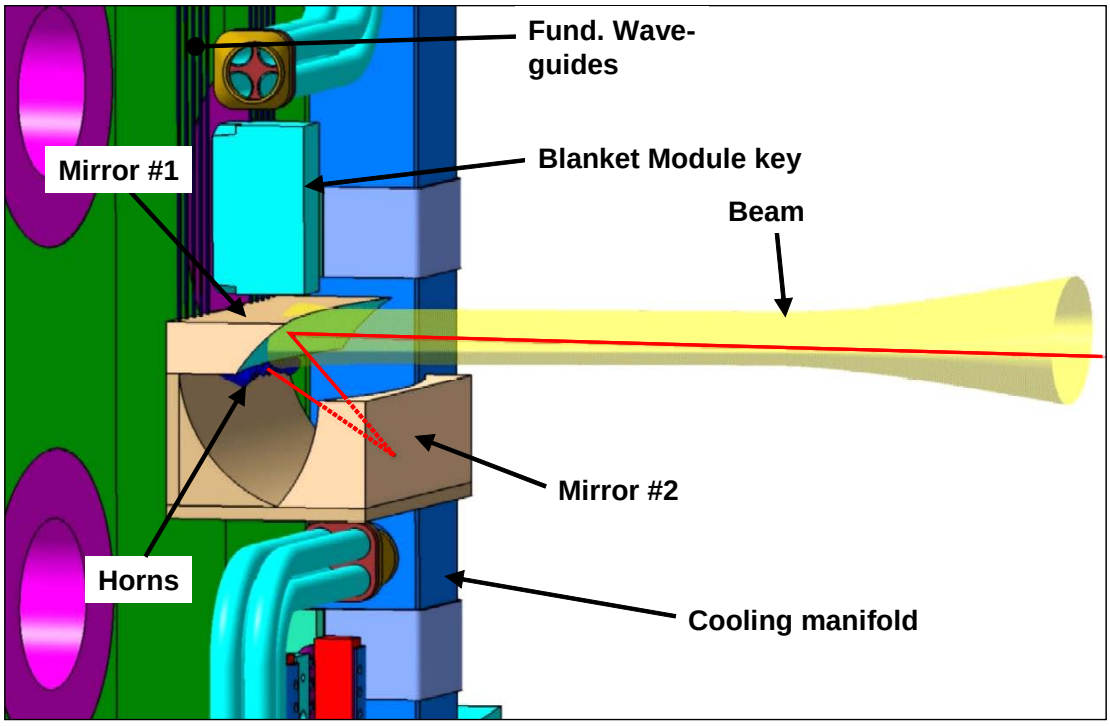

Figure 16. Front end optics of the HFS-FS system mounted on the vacuum vessel wall. For illustration purposes, one of the cooling manifolds is not shown.

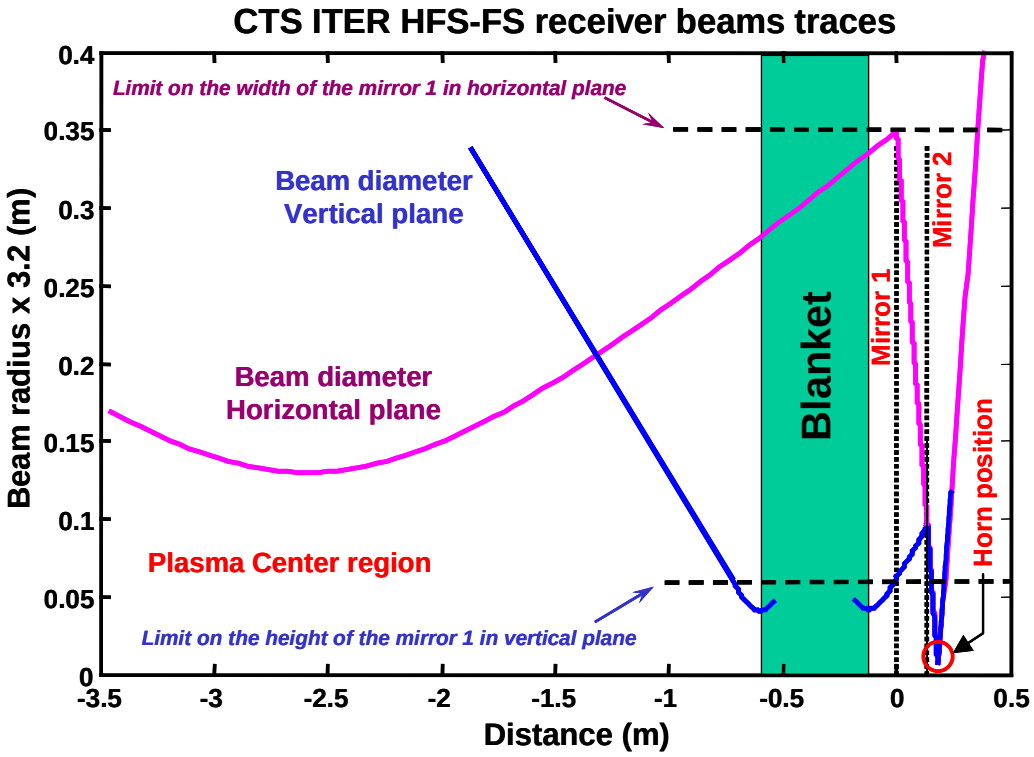

Figure 17. Beam diameters (Gaussian radius × 3.2) as functions of distance for the HFS-FS system. The magenta and blue curve is the beam diameter for the horizontal and vertical dimension, respectively. The vertical dimension of the beam has been chosen to simulate the expanding beam for a vertical gap of 30 mm between the blankets.

3.4 Mock-up model experiment

In order to experimentally investigate the effect of the blanket gap on the microwave beam propagation, a simplified mock-up of the ITER blanket module and the CTS HFS-FS receiver system has been designed, constructed and tested at Risø. The goal of the experiment is to study the effect of the vertical gap dimension on the vertical beam parameters and to investigate the effect of the cut-out as it was mentioned in the Section 3.3. In the following the results from the study are presented.

In the feasibility report it was found that the optimum scattered beam is astigmatic with horizontal beam waist located at the scattering volumes (in the plasma) and expanding in the vertical direction from the blanket vertical gap. The beam diameter in the horizontal plane at the location of the beam waist in the plasma must be smaller than 200 mm to achieve the required radial resolution, as found in Ref. [1]. More importantly, the properties of the beam in the vertical plane depend on the vertical distance between the blankets. As mentioned in the feasibility report, the vertical distance between the blankets have a direct effect on the CTS signal. The conclusion was that the vertical gap between the blankets should be no smaller than 300 mm. This conclusion was based on a 2 dimensional full wave modelling of the emission from a slot aperture antenna. If the gap is smaller the beam is expanding more rapid after the blanket, and the collected CTS signal is therefore a smaller fraction of the possible measuring area.

From the practical point of view, we have investigated the beam dimension independently by two separate experiments under the condition that the beams are purely radial, i.e. perpendicular to the blankets' surface. Two sets of mirror pairs for the mock-up system have been designed to reproduce separately the vertical and horizontal properties of one of the beams in the feasibility report that measures the centre of the plasma. Figure 17 shows the calculated Gaussian beam trace in the vertical (blue) and horizontal (magenta) planes used in the mock-up experiments.

3.4.1 Mock-up

In the design and construction of the mock-up of the CTS ITER HFS-FS receiver system, the following points have been considered:

a) Due to the already existing microwave components (Gunn oscillator, circular corrugated horn, insulator, detector diode, etc) for the 110 GHz frequency at Risø, all dimensions are rescaled by the factor of (λ_{110GHz} / λ_{60GHz}). In this report, distances in the 60 GHz frame will be denoted by a "*" hence for example, $d^* = d \times \lambda_{60GHz} / \lambda_{110GHz}$
b) If the propagation axis is normal to the mirror, each dimension can be separated into two separate set-ups to study the beam properties separately in the 'horizontal' and 'vertical' plane. In other words, the horizontal and vertical system produces a symmetrical beam with the same beam properties as the horizontal and vertical dimensions as the astigmatic beam, respectively.
c) Due to the previous consideration, the experiments were done for cases of the normal incident of the microwave beam to the mirror.

The rescaled values of the beams are as follows:

Horizontal plane:

Beam waist in the plasma = 22 mm;

Beam waist location from the first mirror = 1.41 m;

Vertical plane:

Beam waist at the blanket entrance = 7 mm

Beam waist location from the first mirror = 0.1 m

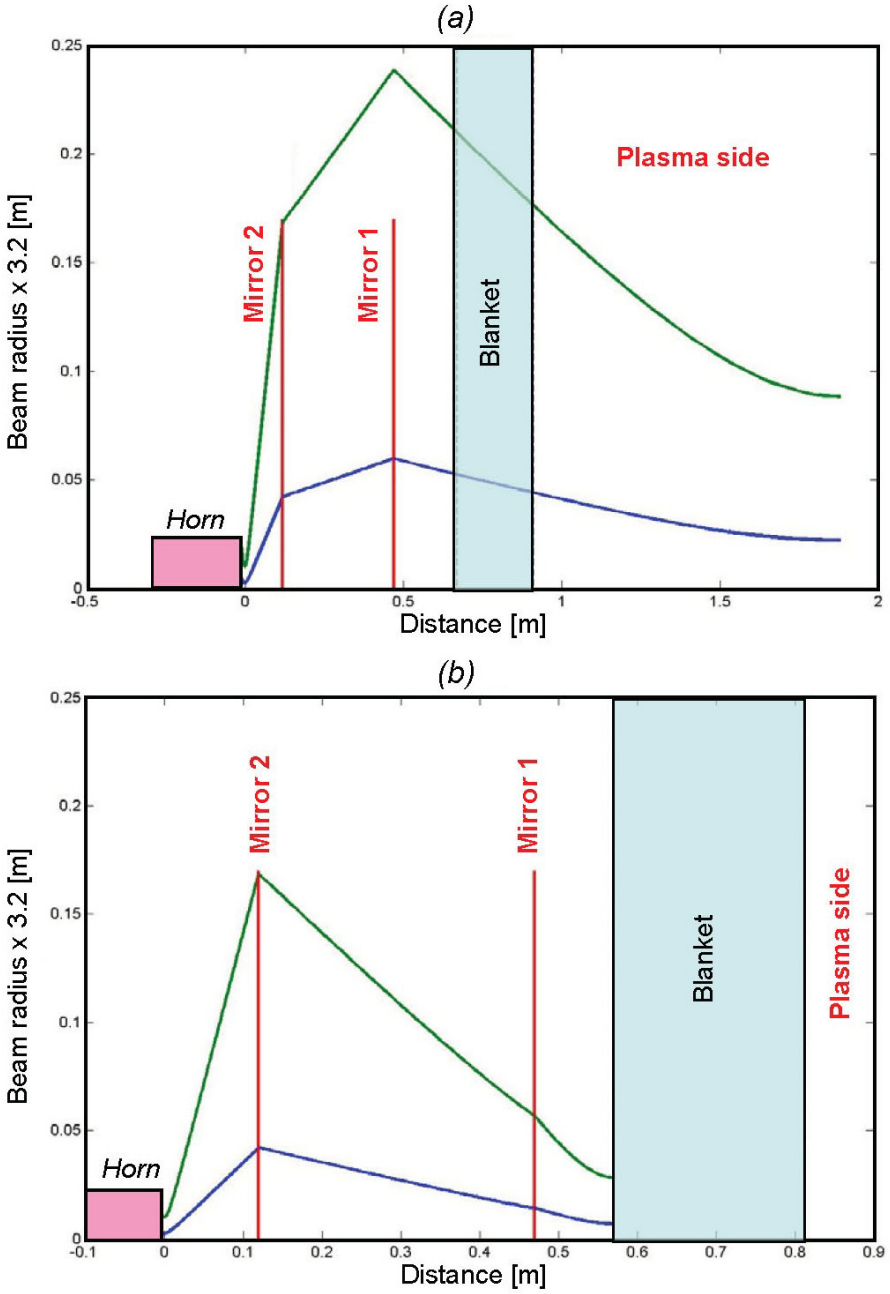

Figure 18. Simulated Gaussian beams for (a) horizontal and (b) vertical planes. Green and blue curves correspond to the full beam width (99.4% of the power transmission) and the beam radius of the Gaussian beam, respectively.

The calculated Gaussian beam profiles are shown in Figure 18, where the beam radius is multiplied with a factor of 3.2 to get the size of the beam containing 99.4 % of the power. Their corresponding 3D images produced by MatLab and CATIA design are also illustrated in Figure 19. Note that the mirror dimension and distance between them do not represent the real case for the CTS HFS-FS receiver since the horn and operating frequency are different.

Quasi-optical mirrors for the mock-up experiments were designed and constructed at Risø. The mirror surfaces for given beam parameters were calculated using Gaussian quasi-optical formulas written in MatLab (Figure 19(a, b)). The mesh of points on the mirror surfaces were

imported into the CAD program CATIA (Figure 19 (c, d)). CATIA was then used to construct the mirror shapes using these distributed points in 3-dimensions. The data was then exported to an ASCII file as input for Risø's computerised cutting tools. The mirrors were cut from standard aluminium. By using the following steps: *MatLab* → *CATIA* → *CNC cutting tools* → *Mirrors*, high quality quasi-optical mirrors with maximum surface roughness less than $1/10^{th}$ of the given wavelength can be produced.

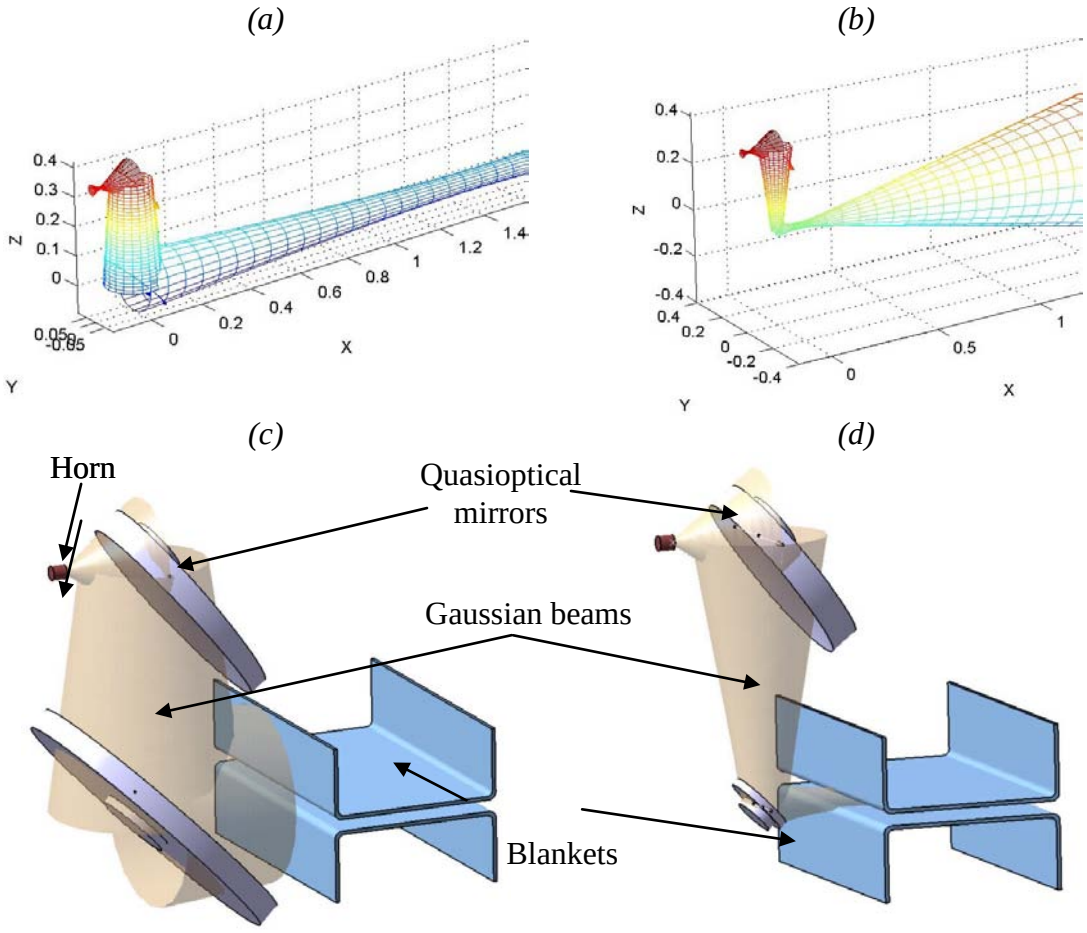

Figure 19. 3D picture of the simulated transmission lines (a, b) and their corresponding CATIA designs (c, d) for the horizontal (a, c) and vertical (b, d) plane set-up.

The rescaled blanket module was also constructed at Risø workshop. The simplified, rectangular shapes with the dimensions of 551×242×100 mm and a radius of curvature at the edge of 16mm were used (Figure 20).

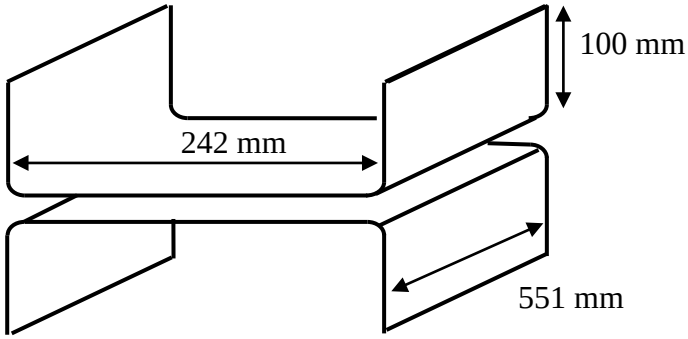

Figure 20: A sketch of the blanket used for the mock-up experiments

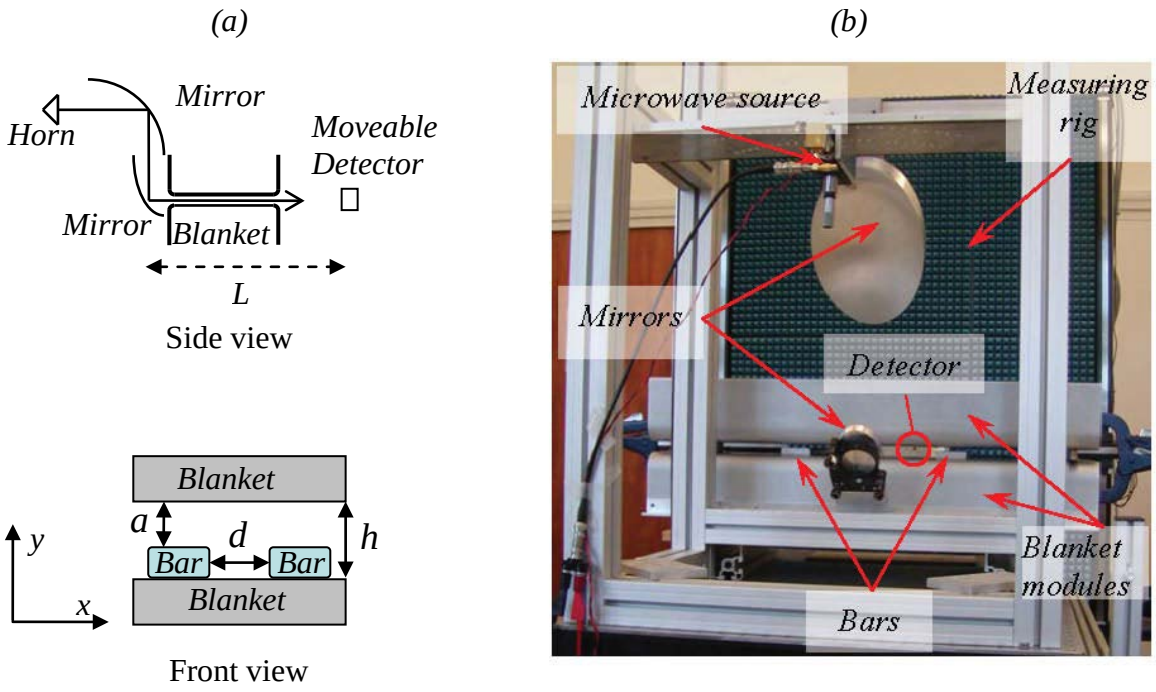

Figure 21 . (a) A sketch of the side and front views of the setup, where L is the distance from the receiver mirror center to the detector. The blanket with the bars inserted - a: the height of the air-gap, d: distance between the bars and h: the height between the blankets (slot height). (b) Setup at Risø seen from the back.

The mock-up is shown in Figure 21. A Gunn oscillator emits radiation through a circular corrugated horn coupled to the mirrors. The mirrors produce the required beam parameters and transmit radiation through the blanket gap. The beam pattern is measured in 2D by a moveable detector, as illustrated in Figure 21**.** To represent the cut-out, two bars with rounded edges have been made and placed parallel to each other and perpendicular to the front of the blanket (Figure 21**(**a)). Hence dimensions *a, h,* and *d* represent the ITER vertical blanket gap, the cut-out height needed for the CTS diagnostic, and the cut-out width, respectively.

3.4.2 Influence of the horizontal dimension of the cut-out in blanket

Since we are not allowed to cut out the whole bottom blanket, the "horizontal experiment" investigates the minimum acceptable size of the cut-out in the lower blanket for a given beam.

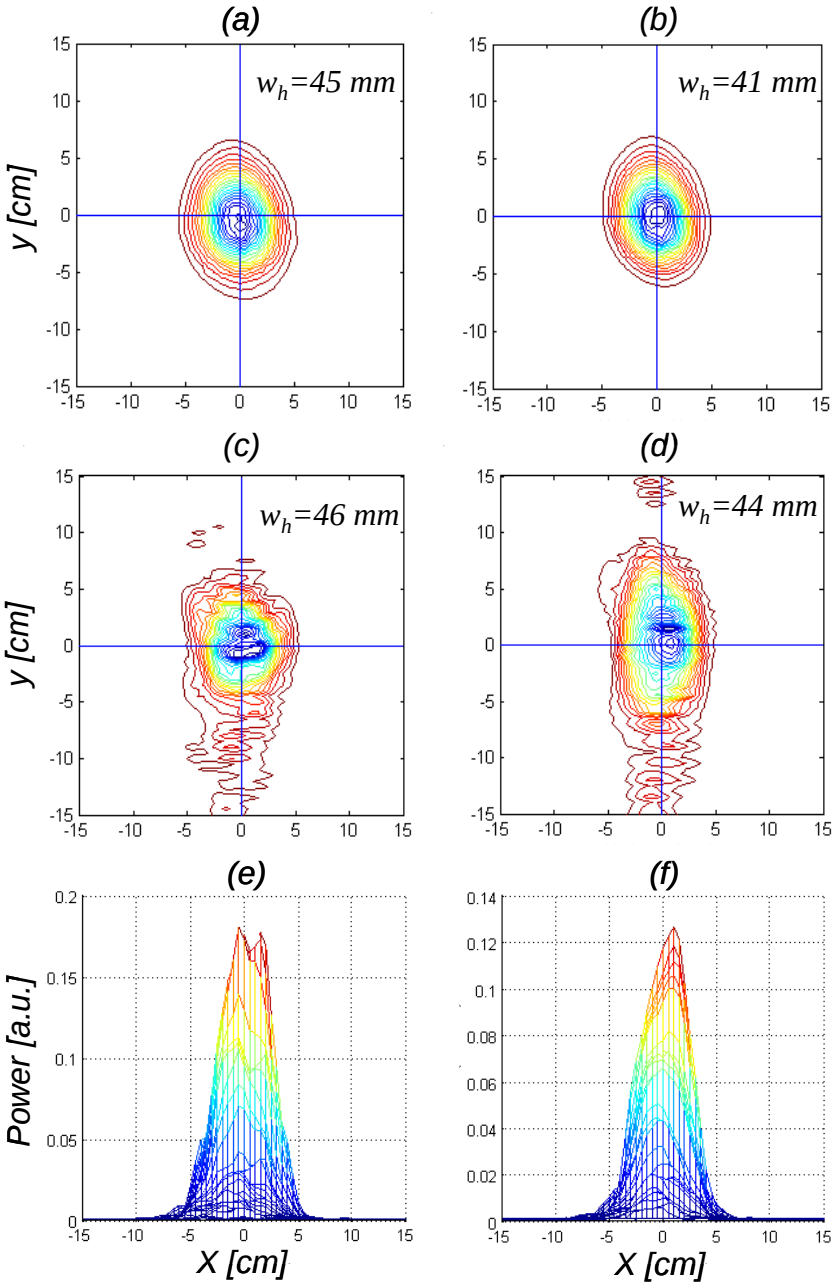

Figure 22. Measured antenna patterns in the horizontal plane during the direct propagation (no blankets were involved) of the beam (a, b) and transmission through the blanket module (c, d). Measurements were performed at two values of L: 0.8 m (a, c) and 1 m (b, d). (e) – (f) represent the profiles of the transmitted through the blankets beam for the cases (c) – (d), respectively.

Figure 22 shows the antenna pattern with and without the blanket at two distances L = 0.8 m and L = 1 m between the receiver mirror and the detector. Two distances are shown to illustrate the beam expansion as a function of distance. The antenna pattern after the blanket modules at L = 1 m illustrates how the beam will look like in the plasma. The rapid expansion in the vertical direction is due to the divergence angle from the slot in the vertical plane and is to be ignored since the optics have been designed only to reproduce the horizontal beam

parameters for this experiment. The lower graphs in the figure show the intensity profile in the horizontal plane. The dips in the power are due to interference in the signal. It is seen that when the beam propagates the beam width decreases in the horizontal plane and the maximum power decreases.

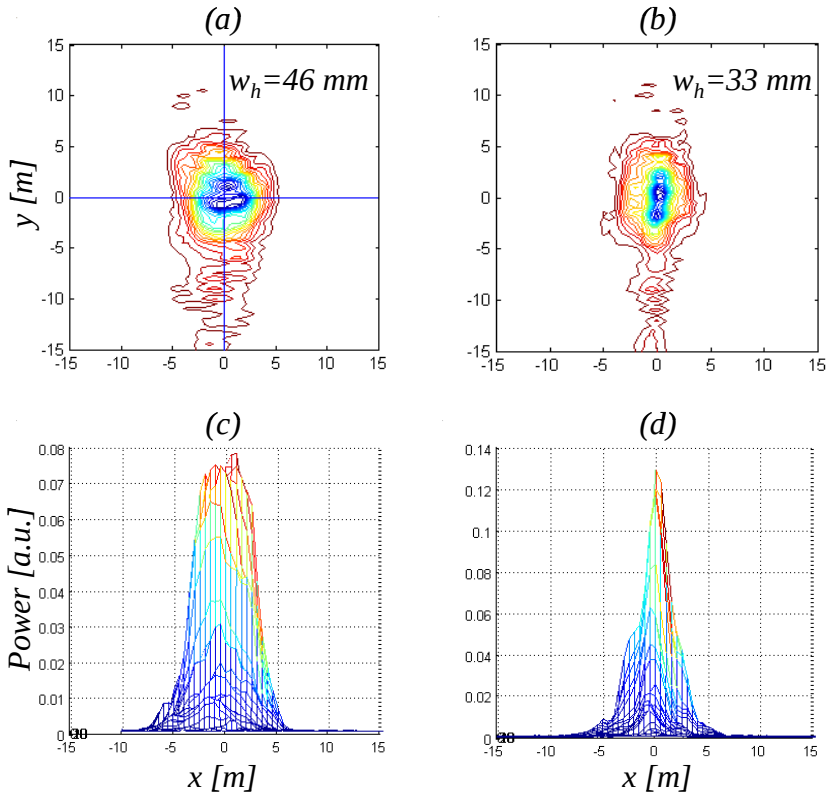

Figure 23. Measured antenna patterns at L = 0.8 mm and for two different values of d*: 350 mm (a) and 150 mm (b). (c) – (d) represent the profiles of the beams corresponding to the (a) – (b) cases, respectively.

To investigate the influence of the cut-out width on the beam, the experiment was done at different values of d. Figure 23 shows the antenna pattern for different sizes of the cut in the blanket. When the distance between the bars is larger than the total beam size (99.4 % of the beam power), the mm-waves are not affected by the bars (Figure 23(a)). When the distance is decreased below the beam diameter the bars behave like a waveguide. Figure 24 shows the Gaussian radius in the horizontal plane as a function of distance between the bars d*, i.e. the distance in the 60 GHz frame. The figure shows that the radius begins to decrease at *d*~300* mm, where the bars act like a waveguide.

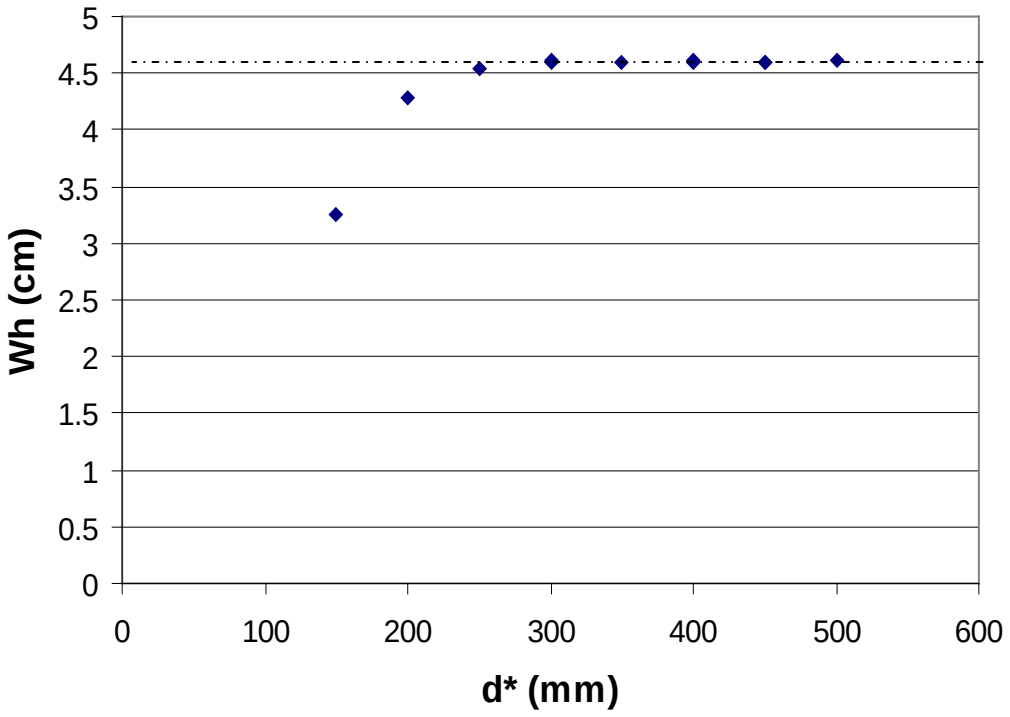

Figure 24. Gaussian radius in the horizontal plane for different distances between the bars at L = 0.8 m. Note that d is scaled to the 60 GHz frame.

It should be noted that the sides (which correspond to the bars in the given study) on the real ITER lower blanket are not parallel to each other and there are oblique angles between the microwave beams transmitted through the blanket module and lower blanket's backside. The viewing angles are 7 to 37 degrees from pure radial direction (Figure 25). To optimize the coupling of all beams, the receiver will be tilted to some angle between these limits in future design. This cut represents the smallest acceptabel cut for optimum measuring capabilities. It has not been verified if it can be constructed like this.

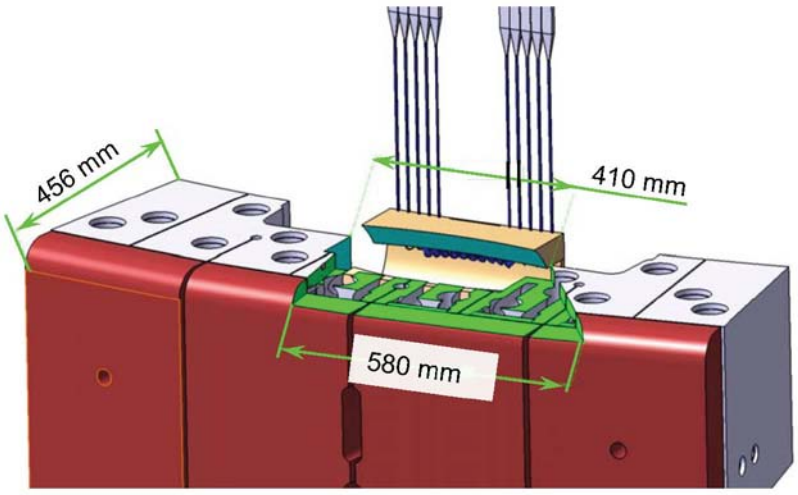

Figure 25. The dimensions of the blanket #3 cut-out for the HFS-FS receiver.

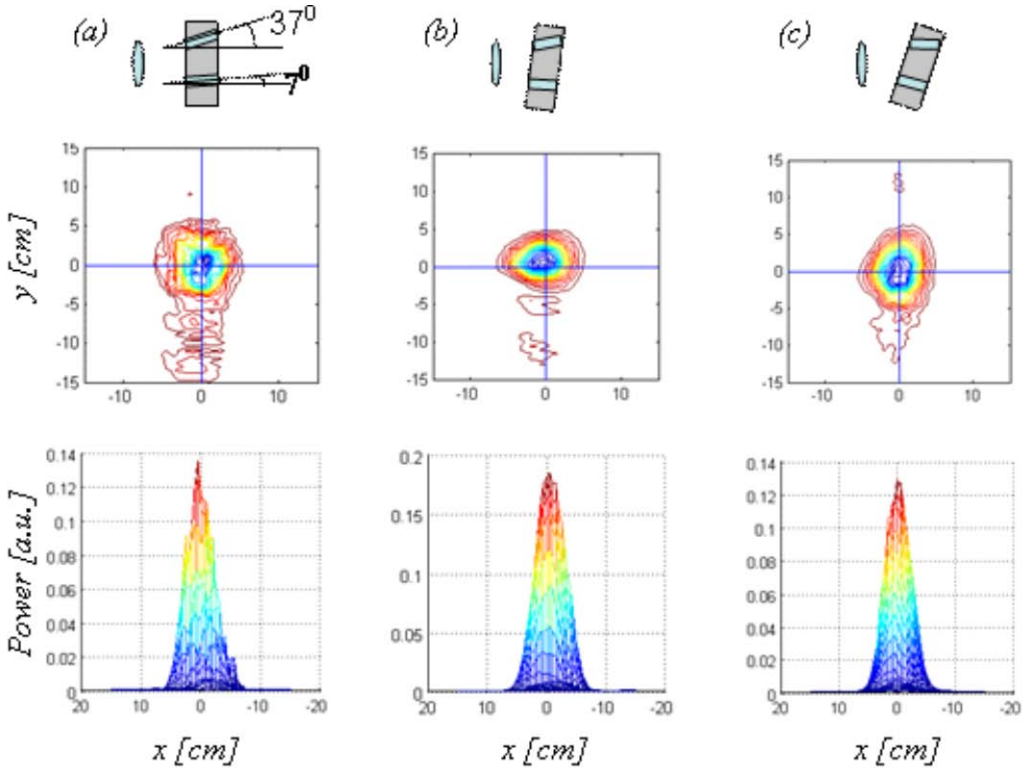

Figure 26. Different angles of the incident beam with respect to the bars.
(a) Beam perpendicular to the blanket front side, (b) rotation of ~ 10 degrees and (c) rotation of ~30 degrees.

In the following experiment the effect of the tilt on the position of the transmitted beam centre in the plasma side and on the beam diameter have been studied.
Figure 26 shows the case with the bars inserted as on ITER and the beam propagates (a) perpendicular to the blanket front end, (b) parallel to the least tilted bar and (c) parallel to the most tilted bar. It has been observed that the antenna pattern can be distorted, when the microwave beam hits the bars (Figure 26 (a)) and otherwise be transmitted like a Gaussian beam. The size of the cut is recommended to be at least the size of the beam, which was found to be the optimal solution in the feasibility report. Note that the signal is collected within a range of ~30 degrees so the cut should have a dimension of as seen on Figure 25.
In conclusion, the angle of incidence does not significantly affect the beam position or the beam diameter. Furthermore, no sidelobes in the horizontal direction were detected. Thus, we can be confident that effect of the blanket module on the beams in the horizontal direction is marginal.

3.4.3 Investigation expanding beam pattern in the vertical dimension

To investigate the influence of the vertical size of the cut-out, the value of h^* was varied. First the parameters of the beam transmitted through the system without blanket module were measured. The beam waist is located just in front of the blanket modules hence coupling to the vertical gap. Using different vertical gap distances, the beam patterns were measured at different distances from the blanket hence calculating the divergence angle. The results show that at h^* = 30 and 20 mm, the divergence α_θ = 7.5° and 9.4°, respectively. It should be noted, however, that in the case of the blanket gap h^*= 20 mm, the same quasi-optical transmission line, as the one designed for the coupling of the beam to the blanket gap h^* = 30 mm, was used.

Full wave calculations presented in the feasibility report [1] have shown that the divergence can be approximated by:

$$\alpha_\theta = \frac{7^\circ \times 6c}{\nu\, h},$$

where c is the speed of light, ν the operating frequency and h (h^* in our case) the size of the gap between the blankets. By using this relation, one can find that the angles should be: 7^0 for h^* = 30 mm, 10.5^0 for h^* = 20 mm. Figure 27 shows the influence of the height h and the distance d on the transmission of the beam through the blanket gaps. As one can see, the edges of the bars become important when the distance between the bars d is comparable with the diameter (Gaussian radius * 3.2) of the beam. Note that the height h*=30 mm is what we recommend but h=20 mm is closer to the height between blankets, at the moment. It is seen that the change in height has an influence on the beam, so it is important that the blanket is placed as accurate as possible, with a tolerance better than 10 mm.

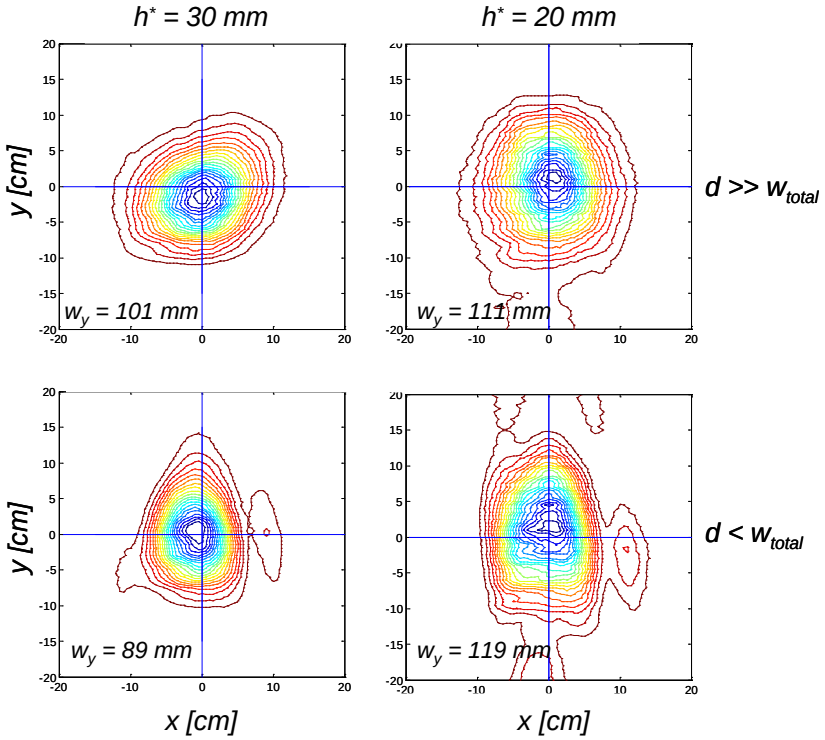

Figure 27 Measured antenna patterns for two different values of h* and for the two cases of d: d >> wtotal - the beam is not affected by the bars (top row) and d < wtotal - the bars work as a waveguide (bottom row).

3.4.4 Alignment

If the beam is misaligned thus entering the slot with an oblique angle, sidelobes can appear. They can cause standing waves in the system. The issue of misaligning the system with respect to the midplane of the blanket module was not investigated thoroughly due to the limited time. So far only observations of the importance of alignment have been made (Figure 28). If the system is misaligned, the sidelobes will appear or power will be lost by reflection at the entrance. Furthermore the beam radius and beam shape will be affected.

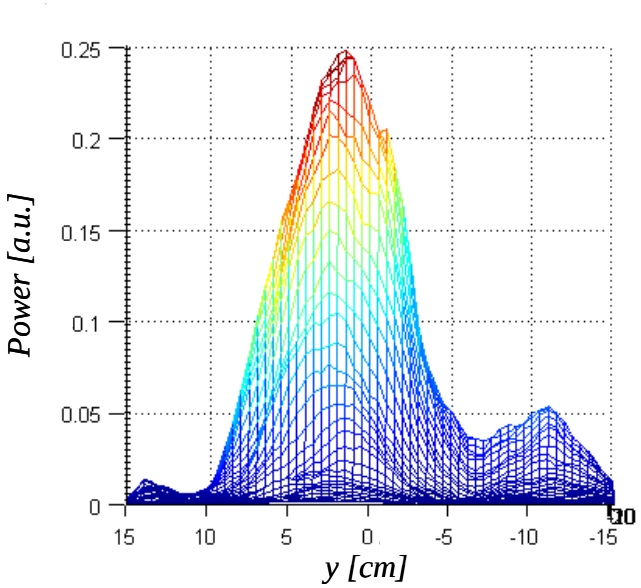

Figure 28. An example of a large misalignment of the beam with respect to the blanket module midplane.

3.4.5 Conclusion

The mock-up experiment has shown that in order to transmit the microwave beam (with the parameters required by the CTS ITER HFS FS receiver) through the ITER blanket module, the horizontal cut in the lower blanket should be at least the same size as the beam diameter. Therefore, incorporating the Gaussian beams in the HFS-FS receiver CATIA model has concluded that for a series of 10 beams in an angular range (7 – 37 degrees), the cut-out should be no smaller than the cut-out shown in Figure 25. The experiments have also confirmed the opening angle as a function of vertical gap from the full wave calculations in the feasibility studies. Therefore, we have shown experimentally that a vertical gap of 30 mm is the minimum value whereby the beam diverging angle is small enough to satisfy the measurement criteria concluded from the feasibility report.

3.5 Numerical calculations to model the beam through the slot.

3.5.1 Introduction

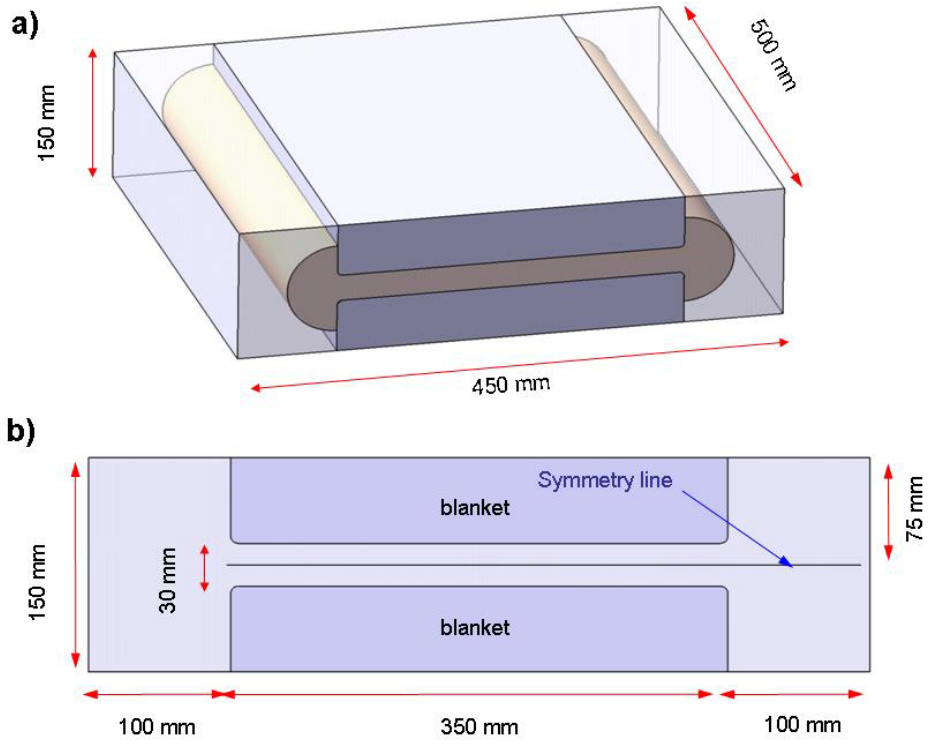

Figure 29. (a) 3D view of the blanket showing the full computational domain, (b) 2D cross section of the domain.

The CTS system is based on a fixed antenna system to collect scattered microwave beams from various positions in the tokamak plasma. On the high field side the bean must pass through the gap between two blanket modules to reach the antenna system. In order to optimise the mirrors, the positions of the horns and the geometry of the transmission gap between the blankets, a finite difference approach has been used to model the beam propagation through the slot. The slot can be optimized based on the the finite difference calculations and investigations of the influence of slot height, radius of curvature of the blankets, tilt and offset of the incidence beam can be performed.
The simplified geometry, including the slot and a region of 150 mm on both sides of the blanket allowing the beam to enter and exit is depicted in Figure 29. The blankets are 500 mm wide and using a wavelength of $\lambda = 5$ mm the total computational domain is: $L_x \times L_y \times L_z = 110\lambda \times 100\lambda \times 30\ \lambda = 330,000\,\lambda^3$. This number can be reduced to half by assuming that the beam is symmetric around the centreline.

Our aim has been to solve the problem from first principle and we have developed a Finite Different scheme solving the wave equations in the Frequency Domain, a so-called FDFD scheme (see next section). The system is very long in terms of wavelength, the blanket itself is $70\,\lambda$ long, and therefore a large number of points per wavelength is needed. It is estimated that approximately 40 points per wavelength are necessary, which, for the *3D* system, correspond to approximately 14,000,000,000 grid points, completely inaccessible for even supercomputers, both in terms of memory acquirement and computational power.

As the full *3D* system is inaccessible, we assume that the problem can be decomposed into a series of *2D* problems by assuming no variations of the slot in the *y*-direction. This assumption is violated when the width of the slot is comparable to the beam width.

The 2D approach (Figure 30), is still too large to solve the problem numerically using a FDFD scheme, and other possibilities have been investigated. One such possibility is to apply third part's software, like FEMLAB (http://www.comsol.dk). This software uses finite element technique having better convergences. FEMLAB has examined the 2D problem and their conclusion is that for the scalar problem it would require a 64-bit computer with 3-4 GB of RAM. Solving the vector problem would increase the memory requirement well above 8 GB of RAM.

3.5.2 Theory

Our aim is to solve the electromagnetic problem using first principle method for a more complete description of the theory and the computer model [1, 2]. As the wave-length is comparable to the variation of the blanket and the slit height analytical simplifications may not be accurate enough, and we thus have to solve Maxwell equations directly. Due to the boundary condition nxE=0 on the surface the Ex and Ez are coupled into the same equation. Ey is decoupled and we can therefore simplify our wave equation to 2D equations, if it is assumed that there is no variation in the y direction.

The starting point is the Maxwell's equations.

Ampere's Law

$$\varepsilon_0 \frac{\partial \vec{E}}{\partial t} = \nabla \times \vec{H} - \vec{J} \qquad (0.1)$$

Faraday's Law

$$\mu_0 \frac{\partial \vec{H}}{\partial t} = -\nabla \times \vec{E} \qquad (0.2)$$

Gauss' law

$$\nabla \cdot \vec{E} = \frac{\rho}{\varepsilon_0} \qquad (0.3)$$

Combining Ampere's law with Faraday's yield

$$\varepsilon_0 \frac{\partial^2 \vec{E}}{\partial t^2} + \nabla \times \frac{1}{\mu_0} \nabla \times \vec{E} = -\frac{\partial \vec{J}}{\partial t} \qquad (0.4)$$

Assuming no free charge and current and using Gauss law transform equation (0.4) into the wave equation

$$\frac{1}{c^2} \frac{\partial^2 \vec{E}}{\partial t^2} = \nabla^2 \vec{E}\,, \qquad (0.5)$$

where $c^2 = \frac{1}{\varepsilon_0 \mu_0}$ and the electric field is a function of both space and time, $\vec{E}(x, y, z, t)$. As we are only regarding one frequency, ω, and since the wave-equation is a linear equation we can without any loss of generality introduce the harmonic time dependence exp(iωt) into equation (0.5)

$$\left(\frac{\omega^2}{c^2} + \nabla^2 \right) \vec{E}(x, y, z) = 0 \qquad (0.6)$$

As mentioned above the full 3D system is too large to be solved directly. We therefore decompose the system into a series of 2D systems by assuming that the solution is periodic in y.

$$\vec{E}(x,y,z) = \sum_{l=-\infty}^{\infty} \vec{E}_l(x,z)\exp\left(\tfrac{2\pi i l}{L_y} y\right) \tag{0.7}$$

Note that this simplification implies that the blanket must not have any variation along the *y*-direction! Inserting the expansion into equation (0.6) yields

$$\sum_{l=-\infty}^{+\infty}\left(\nabla_\perp^2 + \left[(\tfrac{\omega}{c})^2 - (\tfrac{2\pi l}{L_y})^2\right]\right)\vec{E}_l \exp(\tfrac{2\pi i l y}{L_y}) = 0 \tag{0.8}$$

where $\nabla_\perp^2 = \partial_x^2 + \partial_z^2$ and L_y = 500 mm is the length of the domain as seen in Figure 29. Using ortogonality

$$\forall l, \left(\nabla_\perp^2 + \left[(\tfrac{\omega}{c})^2 - (\tfrac{2\pi l}{L_y})^2\right]\right)\vec{E}_l(x,z) = 0 \tag{0.9}$$

In order to solve the equation above we need to employ boundary conditions, which for a Perfect Electric Conductor (PEC) take the form

$$\begin{aligned} &\hat{n}\times\vec{E} = (n_x,0,n_z)\times\left(E_x,E_y,E_z\right) = 0 \Rightarrow \\ &E_y = 0\,,\; n_z E_x - n_x E_z = 0 \end{aligned} \tag{0.10}$$

As the blanket has no variation in y, $n_y = 0$, the equation decouples into a scalar equation only involving E_y and a vector equation involving E_x and E_z.
Since Maxwell's equations are linear we can split-up our solution into two parts; an incident field, $\vec{E}_i$ which is completely unaffected by the blanket and satisfy the Maxwell equations, e.g. an undisturbed Gaussian beam, and a scattered field $\vec{E}_s$. The latter one needs to be calculated from the equation:

$$\begin{aligned} &\forall l, \vec{x}\in\Omega \quad \left[\nabla_\perp + \left[(\tfrac{\omega}{c})^2 - (\tfrac{2\pi l}{L_y})^2\right]\right]\vec{E}_l^S = 0 \\ &\hat{n}\times\vec{E}_l^S = -\hat{n}\times\vec{E}^i \end{aligned} \tag{0.11}$$

3.5.3 Numerical Model

We have developed at numerical scheme which discretize the operator in equation (0.11) using a second order finite different method, where the second order derivatives are approximated by differences between closed neighbouring points on an equidistant grid.

$$\left[\nabla_\perp^2 + \beta_l\right]\vec{E}_l^S = 0 \quad \Rightarrow \quad \underline{\underline{A}}\,\underline{E} = \underline{\underline{A}}\begin{pmatrix}\underline{E}^x\\ \underline{E}^y\\ \underline{E}^x\end{pmatrix} = \underline{B}\,, \tag{0.12}$$

where $\underline{B}$ contains information about the value on the boundary. The matrix, $\underline{\underline{A}}$, is a penta-diagonal matrix with a few exceptions, namely for boundary points which couple the vector elements, $\underline{E}^x$, $\underline{E}^y$ and $\underline{E}^z$.

In order to damp wave propagation on the edge of the computational domain we have implemented a Perfectly Matching Layer (PML). Introducing an electric conductivity and magnetic loss, $\sigma/\varepsilon_0 = \sigma^*/\mu_0$, which only assume non-zero values in a thin layer surrounding

the computational domain. Introducing these losses will change the constant, β_l, in equation (0.12):

$$\beta_l = \left(\frac{\omega}{c}\right)^2 - \frac{2i\omega\sigma}{\varepsilon_0} - \left(\frac{\sigma}{\varepsilon_0}\right)^2 - \left(\frac{2\pi l}{L_y}\right)^2 \qquad (0.13)$$

As the initial condition we use the vector form of the Gaussian beam approximation, which has the following form:

$$\begin{aligned}\vec{E} &= (E_x, 0, E_z) \\ &= \sqrt{\frac{kb}{\pi}}\frac{\omega}{z-ib}\exp\left(ik\frac{x^2}{2(z-ib)} + ikz - i\phi\right)\left(1, 0, -\frac{x}{R} - \frac{ixb}{z^2+b^2}\right)\end{aligned} \qquad (0.14)$$

Where $b = \pi w_o^2 / \lambda$, w_0 being the beam waist.

3.5.4 Results

The model described above has been implemented in Matlab on a standard pc with one GB of RAM and a clock frequency of 2.8 GHz. In Figure 30 we present a simulation, where the left side of the blanket is illuminated by a Gaussian beam with the beam waist of 30 mm and its location at *x* = 0. Only the zero mode of the *y*-direction has been calculated and shown here. For calculating the reflected field we have applied a Perfect Matching Layer with a tightness of 4λ to absorb the energy of this field at the edge of the numerical domain. The edges of the blanket consist of a quarter of a circle with radius 2λ.

The resolution is 20 point per wavelength or 800x300 points in total, note that we here have used the symmetry a *x* = 0. The present simulation is resolved, but if we were to include more or the entire blanket we need to increase the spatial resolution to at least 40 points pr. wave length. The largest possible simulations we have been able to perform on a computer with 2 GB of RAM, is 1600x600 points.

The conclusion is that we have to optimize the code further to make more detailed simulations of the beam propagation through the slot.

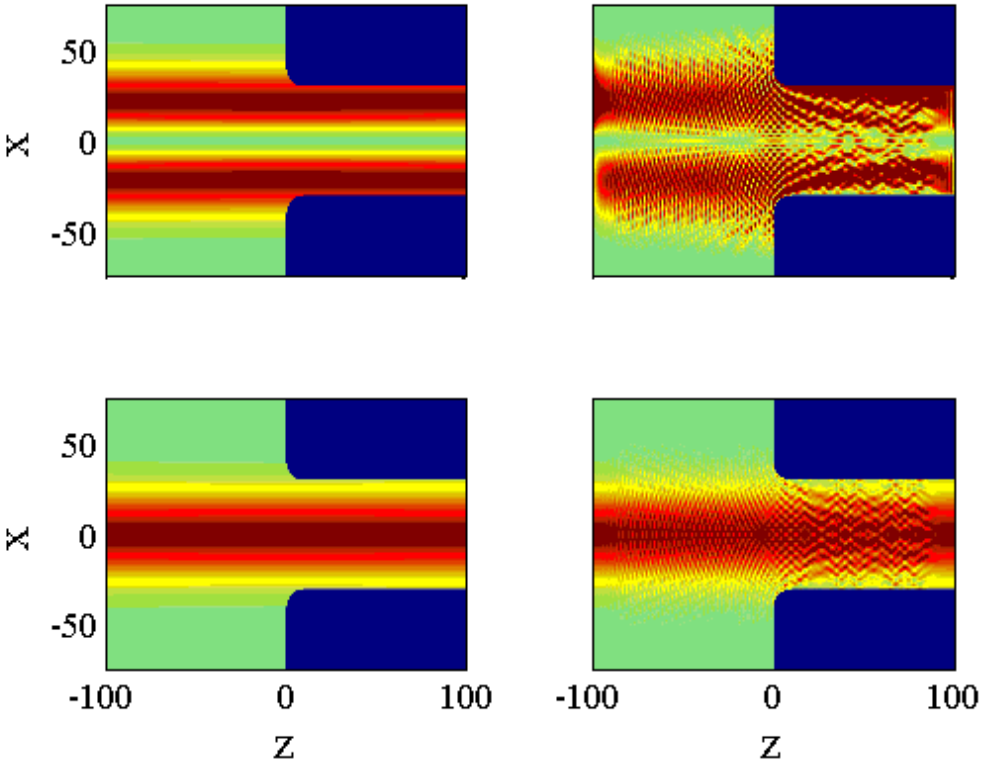

Figure 30. Power distributions for the two vector component of the Gaussian beam, with beam radius of 30 mm and located at z=0, interacting with the blanket. Top row is the z-component and bottom row the x-component. Left column the incident beam and right column the total, i.e. incident and calculated reflected beam. Please note that the power of Ex is approximated 1000 times larger than Ez. Axes are in millimetres.

4 Diagnosing fuel ion ratio and rotation velocity by CTS in ITER

When the resolved fluctuation wave vector, $\mathbf{k}^{\delta} = \mathbf{k}^{s} - \mathbf{k}^{i}$, is near perpendicular to the static magnetic field, $\mathbf{B}$, the bulk ion feature of the CTS spectrum is modulated with the harmonics of all ion species because of weakly damped ion Bernstein modes associated with each of the ion species. A typical spectrum is shown in Figure 31.

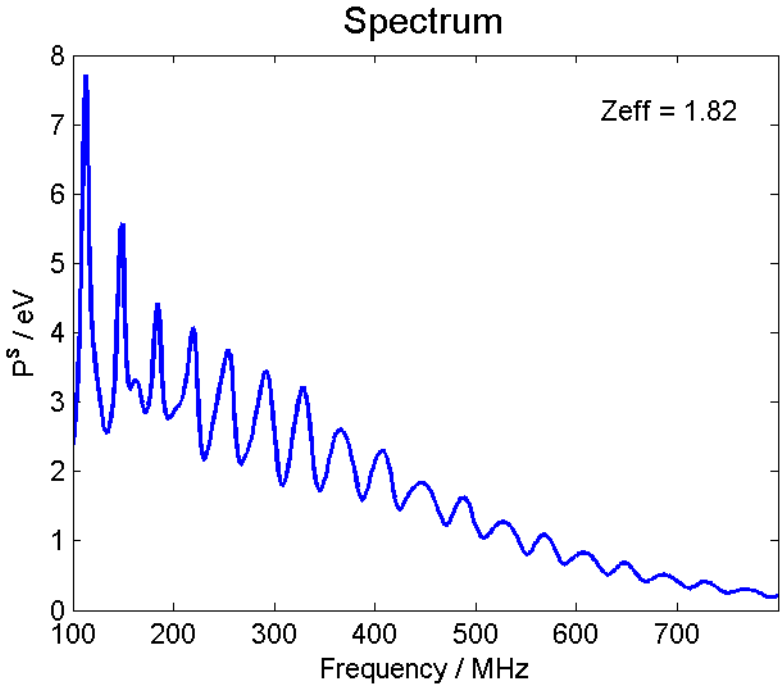

Figure 31 Spectral power density of CTS spectrum. The relevant plasma parameters are given in Table 2 with details of impurity ions in Table 3 and system parameters in Table 4.

The Bernstein modes appear at every harmonic of every ion species. The damping of a Bernstein mode depends on finite Larmor radius effects. The consequence is that the differential variation of the CTS spectrum with the density of one ion specie depends on both its mass and its charge. This is demonstrated in Figure 32 where the spectral variations with the densities of two fictitious ion species with charge 10 and 100, and masses 25 and 250 are considered. The two species have the same temperature. While the two species have the same cyclotron frequency and the Bernstein modes thus appear at the same frequencies it is clearly seen that the spectrum of modes extends to higher harmonics for the lighter ion specie. There are also differences in the detail around each cyclotron harmonic. The consequence is that the two species would in principle be distinguishable in a CTS spectrum given sufficient spectral resolution and signal to noise ratio. Here we are only considering the fuel ion ratio, $R_i = n_T / \left(n_D + n_T \right)$, as a *parameter of interest* while the densities of all other (impurity) ions, which the spectrum does depend on, are not the object of interest here. They do, however, affect the accuracy with which we can estimate the fuel ion ratio and are thus part of the set of *nuisance parameters*. The fact that the differential features of all ion species differ does make it possible to estimate the fuel ion ratio given sufficient spectral resolution and signal to noise ratio. Finding these diagnostic requirements is the object of this investigation.

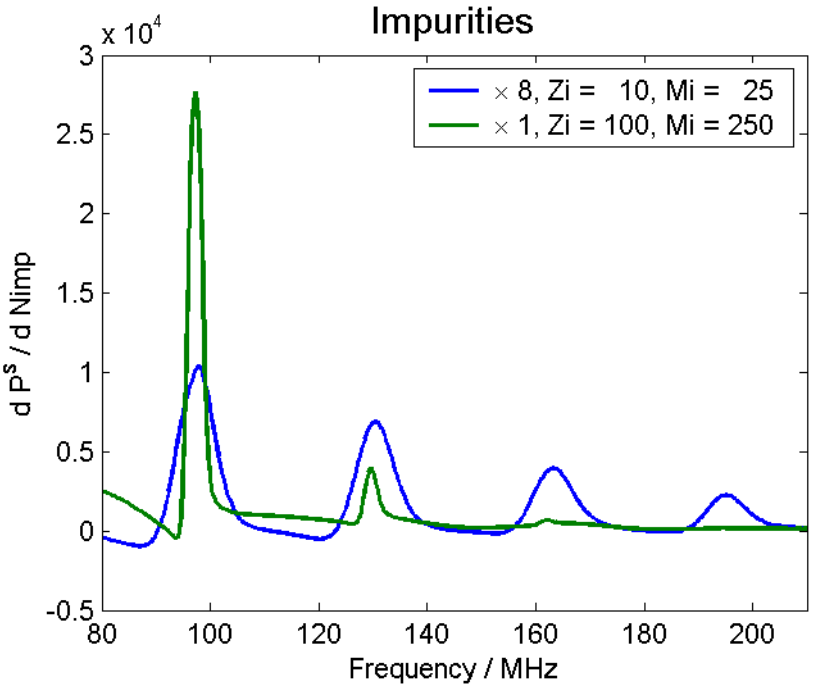

Figure 32 The derivatives of the spectral power density of a CTS spectrum with respect to the densities of two ion species, with charge (mass) 10 (25) and 100 (250) respectively. The curve for the lighter species has been multiplied by 8 to make the scales comparable in this figure. Apart from the impurity ions the plasma is the reference plasma with parameters given in Table 2. The system parameters are given in Table 4.

We will first investigate the possibilities using a probe at 60 GHz, which is below the spectrum of electron cyclotron emissions from the ITER plasma. Subsequently we will investigate the possibilities using a probe at 28 THz (CO_2 laser).
Our reference plasma has the parameters given in Table 2.

Table 2 Reference plasma parameters in scattering volume, and uncertainties in prior information about these parameters.

Quantity	**Symbol**	**Value**	**Uncertainty in prior (STD)**
Magnetic field	B	5.3T	$0.3\times B$
Electron density	n_e	$10^{20}\mathrm{m}^{-3}$	$0.2\times n_e$
Electron temperature	T_e	25 keV	$0.2\times T_e$
Bulk ion temperature	T_i	25 keV	$0.3\times T_i$
Fuel ion ratio	$R_i = n_T/(n_D + n_T)$	0.5	No prior information assumed.
Fast alpha density	n_{fast}	$10^{18}\mathrm{m}^{-3}$	Prior applies to distribution function.
Impurity ion density	$n_{imp}(i)$	See Table 3	$1\times n_{imp}(i)$
Parallel drift velocity	$V_{\parallel}$	10 m/s	200 km/s (very little prior information assumed)
Perpendicular drift velocity	$V_{\perp}$	0	1000 km/s (Essentially no prior information assumed)

These are the plasma parameters in the scattering volume where the probe and receiver beams intersect and the measurement is taken. The plasma profile and the parameters elsewhere in the plasma affect the measurement through refraction and emission. The former we account for through uncertainties in the scattering geometry and plasma parameter values. The emission we account for through the assumed background plasma emissions the CTS signals have to be discriminated against and which reduce the signal to noise ratio of the CTS signals.

Table 3 List of impurity ions in reference plasma. * Tungsten (W) is not fully stripped at a temperature of 25 keV. There will be a distribution of charge states in the range of 60. Here we chose 61 and a mass of 183 as the species which potentially masks the tritium feature most because of their common cyclotron frequency.

Zeff	Impurity ion specie	He	Be	Ar	C	O	Ne	Cu	Kr	W	W	W	W
	Z_{imp}	2	4	18	6	8	10	29	36	61*	62*	65*	74*
	M_{imp}	4	9	40	12	16	20	64	84	183	184	184	184
1.82	$10^3 \times n_{imp}/n_e$	44	20	14	0.1	0.1	0.1	0.02	0.01	5×10^{-4}	0	0	0
2.37	$10^3 \times n_{imp}/n_e$	44	20	14	0.1	0.1	0.1	0.1	0.1	0.1	0	0	0
4.60	$10^3 \times n_{imp}/n_e$	44	20	14	0.5	0.5	0.5	0.5	0.5	0.1	0.1	0.1	0.1

The fast ion population is given 6 degrees of freedom over the velocity range which falls within one side of the bulk ion feature. The purpose of this is to ensure that inference for the fuel ratio is not done on the basis of coarse feature which could be affected by the bulk ion distribution differing from a thermal Maxwellian.
The 60 GHz system could make use of the probe envisioned for the 60 GHz low field side (LFS) fast ion CTS, or better, one slightly offset toroidally from it. It would further make use of a receiver array similar to that of the LFS fast ion CTS, also offset slightly toroidally. The probe power could be much reduced. The present investigations assume probe power of 10 kW as seen in Table 4, which it will be seen below give a very respectable performance. The system is sketched in more detail in Appendix *Sketch of the CTS addition for fuel ion ratio measurements*. The system parameters are given in Table 4.

Table 4. 60 GHz back scattering system parameters and uncertainties in prior information about these parameters.

Quantity	**Symbol**	**Value**	**Uncertainty in prior (STD)**
Probe frequency	ν^{i}	60 GHz	Can be measured to very great accuracy.
Probe power	P^{i}	10 kW	Included in uncertainty in beam overlap.
Integration time	τ	50 ms	
Noise	T_N	100 eV	
Scattering angle	$\theta = \angle\left(\mathbf{k}^{\mathrm{i}}, \mathbf{k}^{\mathrm{s}}\right)$	140°	5°
Resolving angle	$\phi = \angle\left(\mathbf{k}^{\delta}, \mathbf{B}\right)$	88°	5°
Asymmetry angle	ψ	0°	5°
Gaussian beam radius	w	8 cm	Included in uncertainty in beam overlap.

Beam overlap	O_b	Computed from values of w and θ.	$0.4\times O_b$

The integration time with probe on for 50 ms yields the required temporal resolution of 100 ms because of the need for subtracting back ground noise by integrating its spectral power density over a comparable period with the probe off.
With the information defined for the plasma and system we can compute the model spectrum shown in Figure 31. In order to be able to infer the fuel ion ratio the spectrum must be sensitive to the fuel ion ratio. That this is the case is demonstrated by the curve plotted in Figure 33 which represents the differential variation of the spectrum with fuel ion ratio as predicted by our model of the CTS spectrum.

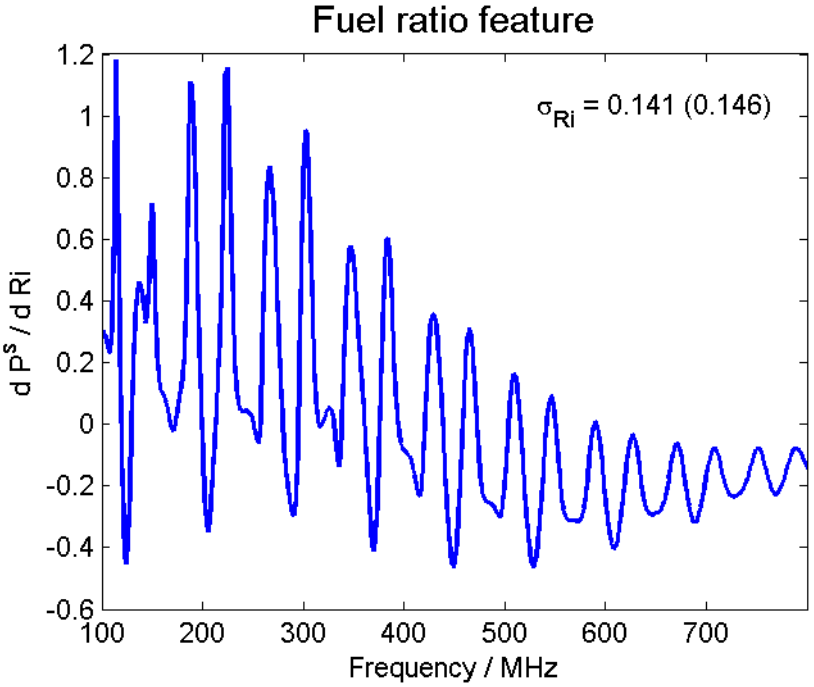

Figure 33 Derivative of the spectral power density of the CTS spectrum with respect to the fuel ion ratio, $\partial P^s / R_i$. Computation assumed reference plasma from Table 2 (Zeff = 1.82) and the 60 GHz back scattering system from Table 4. With the spectral noise, integration time and uncertainties in priors given in these tables the uncertainty in the inferred fuel ion ration is 0.141 (0.146) excluding (including) uncertainties in the fast ion velocity distribution.

The actual inference of the fuel ion ratio is based on fitting the measured spectrum with a model spectrum. Figure 33 indicates that the model spectrum varies with fuel ion ratio and hence indicates that the fitting procedure is going to provide an estimate of the fuel ion ratio, unless there are other parameter variations which can produce that exact same spectral variation. In that case the information on the fuel ion ratio is masked by other nuisance parameters. Generally only partial masking takes place and the fuel ion ratio can be estimated with finite accuracy which depends on the spectral signal to noise ratio, the extent of the masking by nuisance parameters and the uncertainties in prior information available on nuisance parameters.
From the assumed noise and integration time the spectral signal to noise follows. With the added information given in Table 2 and Table 4 on uncertainties in prior information about plasma and system parameters (nuisance parameters) we can estimate the uncertainty in the inferred fuel ion ratio. For the reference plasma (Table 2) and the 60 GHz back scattering system (Table 4) the uncertainties are given in Table 5. Note from Table 3 that 100%

uncertainty is assumed for the impurity ions, i.e. effectively no prior information on impurity ion is assumed, this despite the relatively large number of impurity ion species which are included.

Table 5 Uncertainties (STD) in inferred fuel ion ratio for the reference plasma (Zeff = 1.82) and two plasmas with increased impurity ion densities.

Zeff	1.82	2.37	4.60
σ_{Ri}	0.146	0.151	0.138

As with the fast ion measurements, the spatial resolution would be in the range of one tenth the minor radius (a/10), assuming 10 or more receivers as in the case of the fast ion CTS.

The ability to measure the fuel ion ratio has not been demonstrated experimentally. It could be attempted on the existing CTS diagnostic on TEXTOR or the new CTS diagnostic on ASDEX Upgrade. In both case investments in means to provide high spectral resolution of the bulk ion feature would have to be made. The limited spectral range makes it possible to consider spectral resolution by Fourier transformation of the full bandwidth signal digitized at the rate of 1.5 Giga samples per second. With such an approach the spectral resolution is limited by the sampling time and the signal to noise ratio. The former could be 50 ms giving a spectral resolution of 20 Hz, which is far better than required. The achievable signal to noise ratio thus sets the limit on the usefully achievable spectral resolution. That assumption underlies the numerical investigations made here. Demonstration on current devices would confirm the principle. Comparing the experimental observations with model predictions of the type presented here, could confirm the numerical modeling and thus give extra confidence to the present predictions of success of such a system for ITER. Also demonstration on current devices would undoubtedly give valuable experience and added insights.

The bulk ion feature of the CTS spectrum is sensitive to the ion drift velocity in the direction of the resolved fluctuation wave vector, $\mathbf{k}^{\delta} = \mathbf{k}^{\mathrm{s}} - \mathbf{k}^{\mathrm{i}}$. This implies that the bulk ion drift velocity in the direction of $\mathbf{k}^{\delta}$ can be inferred from the CTS spectrum. For the fast ion or fuel ion ratio LFS-BS systems $\mathbf{k}^{\delta}$ is essentially radial and near the mid plane, so it includes a very small poloidal component. Measuring the poloidal velocity component would thus require a different scattering geometry from the one considered for the fast ion and fuel ion ratio LFS-BS systems. One solution would be vertically displaced scattering volumes at a major radius close to the plasma centre. The spatial resolution could in this case be finer than one tenth the minor radius (a/10). This geometry would, however, require a separate probe beam for each measurement location. The toroidal drift velocity could, on the other hand, be measured using the previously discussed HFS-FS fast ion CTS system.

Considering first the case of $\mathbf{k}^{\delta}$ near perpendicular to the magnetic field with system and plasma parameters as considered above. For this case the derivative of the CTS spectral power density with respect to bulk ion drift velocity is as shown in Figure 34, which shows that the spectrum is very sensitive to the drift velocity and hence that the drift velocity should be inferable with considerable accuracy. This is essentially because the entire bulk ion feature, which for near perpendicular scattering is highly structured, is Doppler shifted by the drift.

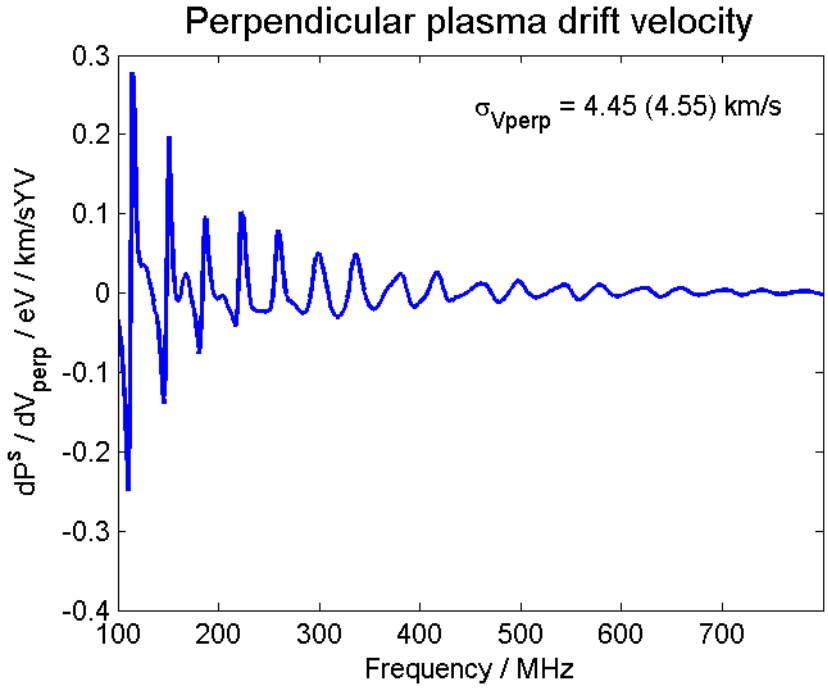

Figure 34 Derivative of the spectral power density of the CTS spectrum with respect to the drift velocity perpendicular to the magnetic field, $\partial P^s / V_\perp$. Computation assumed reference plasma from Table 2 (Zeff = 1.82) and the 60 GHz back scattering system from Table 4. With the spectral noise, integration time and uncertainties in priors given in these tables the uncertainty in the inferred drift velocity is 4.45 (4.55) km/s, excluding (including) uncertainties in the fast ion velocity distribution.

For the reference plasma with parameters defined in Table 2, and the 60 GHz back scattering system with parameters given in Table 4, the uncertainties in the inferred perpendicular drift velocity are given in Table 6.

Table 6 Uncertainties (STD) in inferred fuel ion ratio for the reference plasma (Zeff = 1.82) and two plasmas with increased impurity ion densities.

Zeff	1.82	2.37	4.60
$\sigma_{V_\perp}$ / km/s	4.55	4.53	4.18

Measurements of the toroidal rotation velocity requires a scattering geometry with the resolved fluctuation wave vector, $\mathbf{k}^\delta$, mainly in the toroidal direction and with a negligible component in the poloidal direction. This is achievable with the forward scattering geometry also proposed for the fast ion CTS, with probe from the low field side mid plane and receivers on the high field side, viewing the plasma through the slot between blanket modules. With this geometry and other system parameters as above the uncertainty in inferred toroidal drift velocity is in the range of 20 km/s. The main source of uncertainty is the fast ion distribution. With less conservative assumptions on the masking influence of the fast ions distribution the uncertainty can be reduced down to below 10 km/s. The uncertainties are not significantly affected by impurity ions.

We turn now to measurements of the fuel ion ratio using a 28 THz probe, that is, a CO_2 laser. The scattering (measurements) volume is generally very elongated because of small scattering angles, which are less than one degree. It appears therefore that to maintain reasonably uniform conditions throughout the scattering volume, including the crucial angle between the resolved fluctuation wave vector, $\mathbf{k}^\delta$, and the magnetic field, it is necessary to use a geometry where the beams are near tangent to the toroidal direction in the scattering volume. Even in

this geometry it is necessary to pay attention to the length of the scattering volume, which can be reduced by increasing the scattering angle. At larger scattering angles the finite Larmor radius effects are less pronounced in differentiating between species with identical charge to mass ratios. The consequence is a poor accuracy on the inferred fuel ion ratio.

Table 7 Accuracy of inferred fuel ratio and length of measurement (scattering) volume for a range of scattering angles for a 28 THz far forward scattering system. It is assumed that the probe has a pulse length of 1 micro second and that the antenna noise temperature of the receiver is 5 eV. The Gaussian radii of the probe and receiver beams are assumed to be 1 cm.

Scattering angle,	0.6°	0.4°	0.3°	0.2°
Length of scattering volume	3.3 m	5 m	6.7 m	10 m
σ_{Ri} (Pulse energy = 1 joule)	4.8	4.2	3.9	1.1
σ_{Ri} (Pulse energy = 10 joule)	3.9	3.2	2.0	0.56
σ_{Ri} (Pulse energy = 100 joule)	3.5	2.9	1.7	0.47

The length of the scattering volume can be reduced and the signal to noise ratio improved by reducing the beam widths. This does, however, lead to a broadened distribution of resolved fluctuation wave vectors which needs to be taken into account when considering this course.

In conclusion, it appears that a 60 GHz CTS system can measure the fuel ion ratio and poloidal and toroidal drift velocities with the required accuracy. It is not obvious that the fuel ion ratio can be estimated with the required accuracy using a probe at 28 THz. It is likely that useful information on drift velocities can be provided by a 28 THz system.

5 Future tasks on R&D, design and performance assessment

In the conceptual design report for an ITER Fast Ion Collective Thomson Scattering System (Contract 01.654) it was concluded that the of the 60 GHz CTS system can be integrated into ITER with existing and near term technologies. This conclusion has not been changed by the more detailed design work for the present report. The work has mainly been concentrated on investigations of the optimum design for the receiver antenna system on the HFS. Some modifications to the ITER components need to be done to accommodate the CTS. The most significant one is the vertical gap required between the HFS blanket modules where the HFS-FS system is measuring.

For resolving some of the problems with integrating the antenna system on the HFS, we have made a simple mock-up experiment, consisting of a model of two blanket plates and a mirror system in order to transmit the beam through the slot between these blanket plates. A measuring rack with a microwave detector diode can measure the radiation pattern in a plane perpendicular to the beam. From the information about the beam transmission through the slot to the plasma, and from calculations of beam traces through the plasma, it is possible to estimate the performance of the diagnostic.
The work for this contract has shown that a full 3-dimensional numerical simulation of the electromagnetic wave transmission is not possible even if the ITER plasma is not included. The problem is that to simulate the distance from the horn through two mirrors and through the slot between two blanket modules to the plasma edge will require more grid points than it is possible to handle with present computers. Specialists in the field estimate that it is

necessary to have 40 grid points per wavelength in order to keep the correct phase information.

The present work has as the main result shown that it is possible to accommodate an antenna system on the HFS, and that it is possible to transmit an adequate signal to the antennae.

R&D should focus on components and issues that are critical to the viability of CTS on ITER. The most important technical issues which need further R&D particular to the CTS, and which will be necessary to perform before a full-scale model and the final design of the diagnostic can be made are the following:

1. Development of codes for model calculation for optimisation of mirrors will be necessary. The physics feasibility study has shown that astigmatic beams are needed to satisfy the ITER measurement requirements for the fast alpha particles. Hence it is necessary to upgrade the codes to calculate the mirror shapes for such beams in 3 dimensions. The calculations of the optimum shapes of the antenna mirrors are non-trivial due to the fact that 8 or 10 beams have to be transmitted on the same mirror.

2. Development of an improved mock-up experiment for testing front-end components. The mock-up has to be equipped with new shaped mirrors that will transmit astigmatic beams in3D, a more realistic blanket model, a better alignment system including a mechanism for precise motion of mirrors and a faster motion of the detector on the radiation pattern rack. This will give the possibility to optimise the high field side antenna system by testing various mirrors and horn systems. An assessment of the importance of blanket edge shapes, the acceptable tolerances for positions of antenna system and blanket modules should also be studied. The mock-up experiment could also give valuable information for the assessment of alignment and conditioning issues. This study should also assess acceptable tolerances for misalignment.

3. Studies of key mm-wave components and other critical components and issues, including investigation of the relative merits of circular and rectangular horns for the CTS receivers, and optimisation of the mirrors for transmission of beams from a set of horns.

On the longer term it is foreseen that the following design and R&D tasks have to be performed

1. Building and testing a full-scale antenna model.
2. Investigations of passive and active cooling of the front-end components.
3. Development of prototypes of some special receiver components.
4. Develop concepts for calibration methods for both the HFS and the LFS systems,
5. Material investigations including assessment of the system performance due to material expansions, misalignments, stress loads etc.
6. Technical feasibility of transferring 10-20 waveguide vacuum breaks through ports.
7. Calculations of final design; Thermo-mechanical calculations, neutronics (heating, activation, and streaming), cooling, and, remote handling concepts.
8. Design and test of receiver unit and data acquisition system. These systems can be made by current technology. However, the optimum final design will depend on the progress in data acquisition technology, and should not be finalized before absolutely necessary.

A detailed engineering design of the CTS diagnostic for ITER including the design task mentioned above has to be performed as soon as possible.

6 Documentation

Throughout the execution of this contract there have been extensive consultations with the ITER IT. To facilitate the updating of ITER documentation this report will be provided to the ITER IT. All relevant drawings have already been transmitted to ITER IT.
The results in this report do not change any of the conclusions obtained in the feasibility study [1]. The scattering simulations and the calculations of the resolving power presented in section 2 are updated to the present mirror design as regards to the calculations presented in the conceptual design report [2] section 3, whereas the design requirements presentented in that section have not been changed. All design drawings in [2] have been further devloped, but a detailed engineering design still has to be carried out.

Acknowledgements

We would like to thank the ITER and EFDA staff for their useful help and comments particularly, Chris Walker, George Vayakis, David Campbell, Damian Lockley, and Christian Ingesson.

Appendix: Sketch of the CTS addition for fuel ion ratio measurements

The CTS for measuring the fuel ion ratio makes use of the same probe, or nearly same probe, as the back scattering fast ion CTS (LFS-BS) and has a similar arrangement of receiver beams, only slightly offset toroidally to give a scattering geometry which resolves the fluctuations closer to perpendicular to the magnetic field than the fast ion LFS-BS does. Thus the scattering geometry is as sketched in Figure 35.

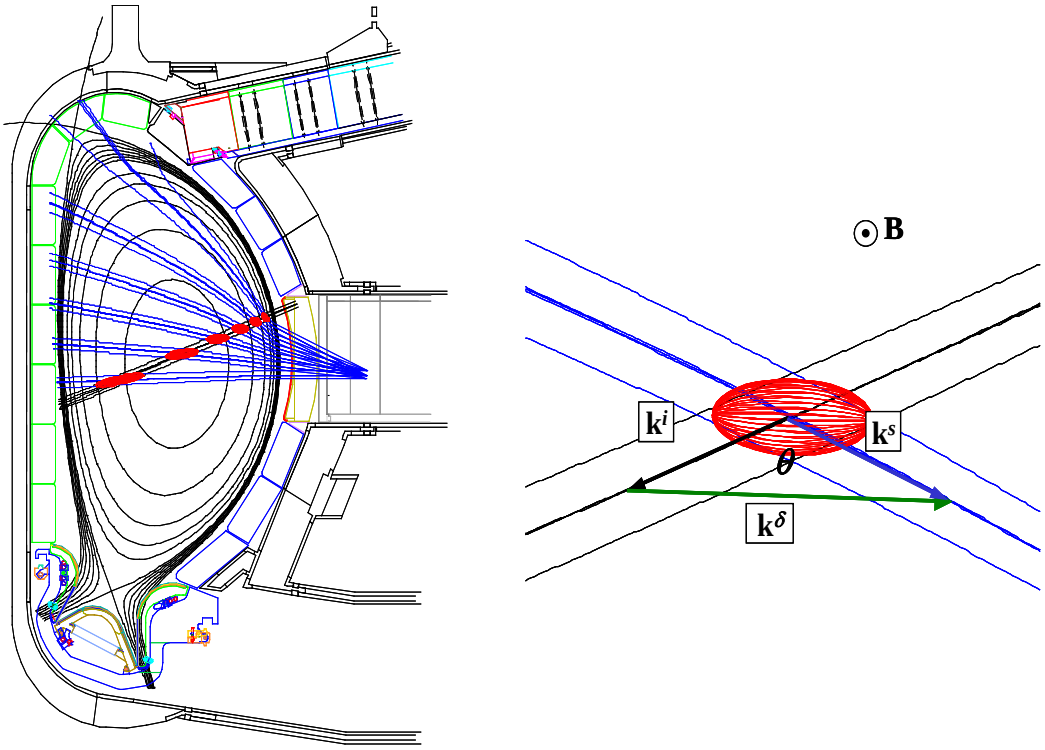

(a) **(b)**

Figure 35 Sketch of the scattering geometry for the CTS for measuring fuel ion ratio in ITER. Left figure shows a poloidal cross section of the ITER vacuum vessel, the probe beam in black emanating from the upper part of the mid plane port, multiple receiver beams in blue, 6 shown here, but 10 or 16 are envisioned. The scattering volumes appearing where the probe beam intersects a receiver beam are sketched as red ellipsoids. The right figure shows one scattering volume, the wave vectors of the incident probe radiation in black and the received scattered radiation in blue. The wave vector of the resolved fluctuations is shown in green. The magnetic field is out of the page. The wave vector of the resolved fluctuations is near orthogonal to the magnetic field.

The multiple receiver beams are to be realized using an array of horns viewing the plasma via a common quasi optical mirror, shared with the fast ion LFS-BS CTS system. The concept is sketched in Figure 36. Figure 37and Figure 38 show CATIA drawing of the current design of the two LFS-BS CTS systems, one for fast ion detection, the other for measuring fuel ion ratios resolved spatially with essentially the same resolution as the fast ion LFS-BS.

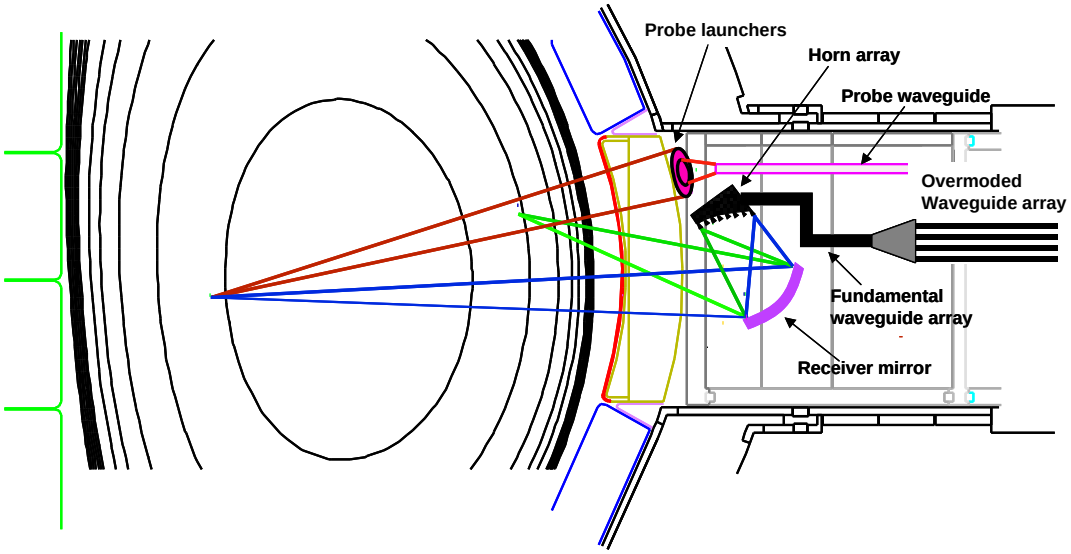

Figure 36 Polidal cross section of part of the ITER vacuum vessel, contours of flux function defining the location of the plasma, probe beam in red, two receiver beams in respectively blue and green, quasi optical receiver mirror, horn array and wave guide transmission lines.

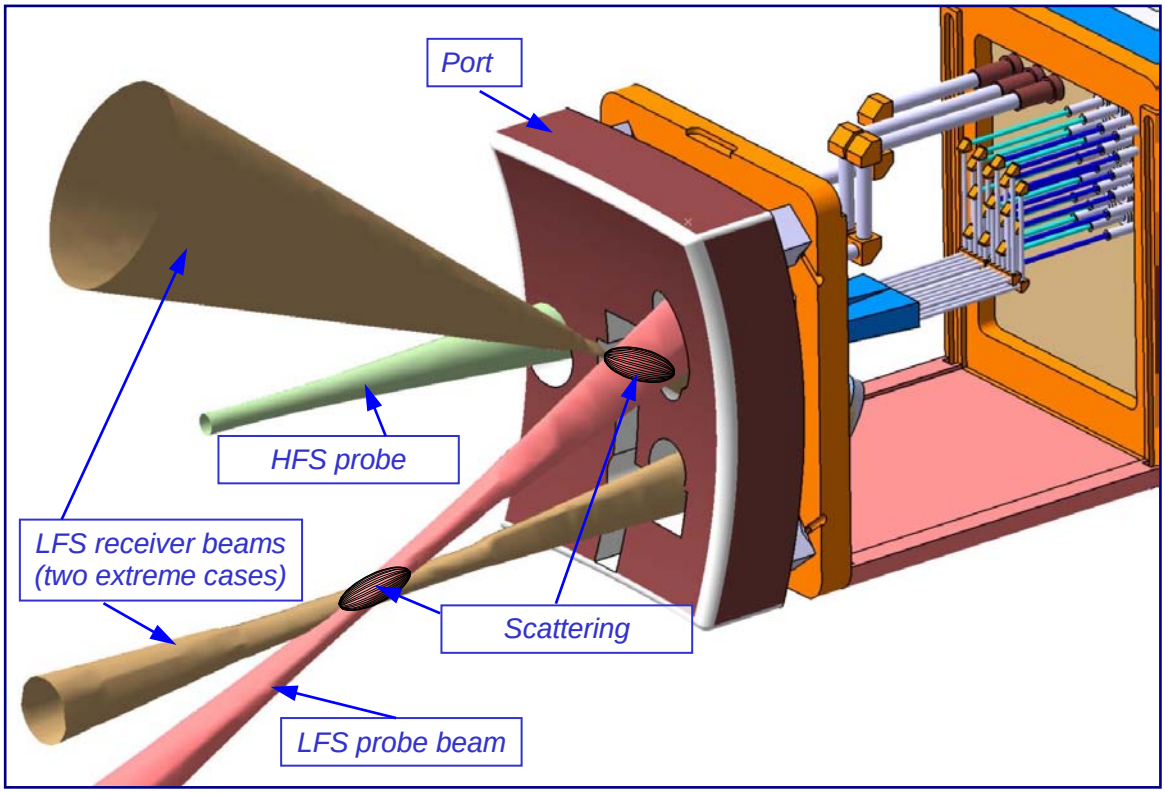

Figure 37 CATIA drawing of fast ion and fuel ion ratio CTS systems seen from the plasma side. The probe beam is in pink, two receiver beams in light brown. Scattering volumes at beam intersections are shown as hashed ellipsoids. Thin waveguides seen in port plug are for the receivers. The three fat wave guides are for the HFS-FS fast ions CTS, the LFS-BS fast ion CTS and the LFS-BS fuel ion ratio CTS.

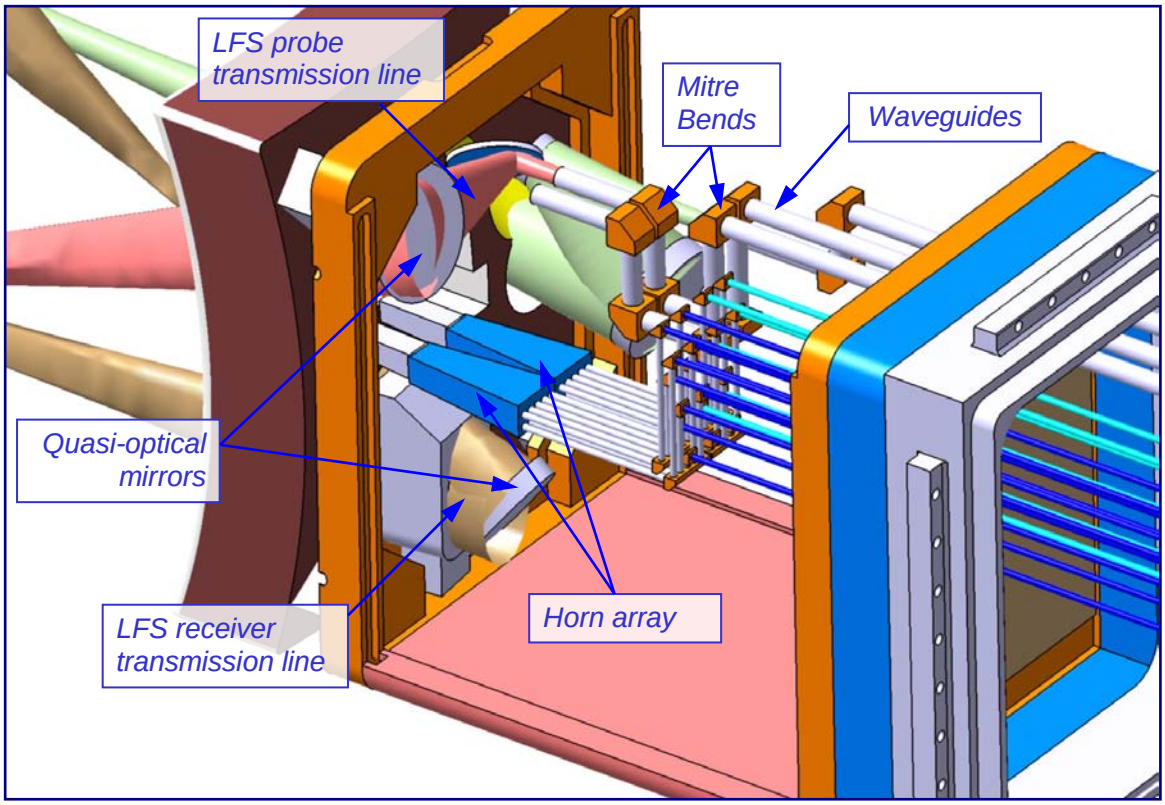

Figure 38 CATIA drawing of fast ion and fuel ion ratio CTS systems seen from the port side. The probe beam is in pink, two receiver beams in light brown. Thin waveguides seen in port plug are for the receivers. The three fat wave guides are for the HFS-FS fast ions CTS, the LFS-BS fast ion CTS and the LFS-BS fuel ion ratio CTS. The two LFS-BS systems launch their probes off the same quasi optical mirror. There are two sets of horn arrays, visible here. One is for the fast LFS-BS fast ion CTS the other for the LFS-BS fuel ion ration CTS. Both sets of receiver horns view the plasma via the same quasi optical mirror.

References

1. H. Bindslev, F. Meo, S. Korsholm, ITER Fast Ion Collective Thomson Scattering, Feasibility study, part of the Final Report of EFDA Contract 01.654

2. F. Meo, H. Bindslev, S. Korsholm, ITER Fast Ion Collective Thomson Scattering, Conceptual design of 60 GHz system, part of the Final Report of EFDA Contract 01.654

3. ITER operating scenario data base, http://efdasql.ipp.mpg.de/saibene/ITER_Eq_Restricted/equilibria_index.htm (password protected), Yuri Gribov, website maintained by Gabriella Saibene

4. CAD/CAM/CAE commercial software suite developed by Dassault Systems and marketed world-wide by IBM. www.ibm.com/catia

5. Goldsmith, P. F., Quasioptical systems. Gaussian beam, quasioptical propagation and applications, IEEE Press.

6. Hiromasa, Iida, iidah@itergps.naka.jaeri.go.jp, private communication, Naka, Japan

7. Bondeson, Anders, Rylander, Thomas, Ingelström, Par, Computational Electromagnetics, 2005, ISBN: 0-387-26158-3

8. Allen Taflov, Computational Electrodynamics: The Finite-Difference Time-Domain Method, 1995 Artech House, INC. ISBN 0-89006-792-9